



HAL
open science

Molten Salts-Driven Discovery of a Polar Mixed-Anion 3D framework at the nanoscale: $Zn_4Si_2O_7Cl_2$, Charge Transport and Photoelectrocatalytic Water Splitting

Ram Kumar, Yang Song, Anissa Ghoridi, Philippe Boullay, Gwenaëlle Rousse, Christel Gervais, Cristina Coelho Diogo, Houria Kabbour, Capucine Sassoïe, Patricia Beaunier, et al.

► To cite this version:

Ram Kumar, Yang Song, Anissa Ghoridi, Philippe Boullay, Gwenaëlle Rousse, et al.. Molten Salts-Driven Discovery of a Polar Mixed-Anion 3D framework at the nanoscale: $Zn_4Si_2O_7Cl_2$, Charge Transport and Photoelectrocatalytic Water Splitting. *Angewandte Chemie*, 2023, 10.1002/ange.202303487 . hal-04070975

HAL Id: hal-04070975

<https://hal.science/hal-04070975v1>

Submitted on 16 Apr 2023

HAL is a multi-disciplinary open access archive for the deposit and dissemination of scientific research documents, whether they are published or not. The documents may come from teaching and research institutions in France or abroad, or from public or private research centers.

L'archive ouverte pluridisciplinaire **HAL**, est destinée au dépôt et à la diffusion de documents scientifiques de niveau recherche, publiés ou non, émanant des établissements d'enseignement et de recherche français ou étrangers, des laboratoires publics ou privés.



Distributed under a Creative Commons Attribution 4.0 International License

Molten Salts-Driven Discovery of a Polar Mixed-Anion 3D framework at the nanoscale: $Zn_4Si_2O_7Cl_2$, Charge Transport and Photoelectrocatalytic Water Splitting

Ram Kumar,^[a] Yang Song,^[a] Anissa Ghoridi,^[a] Philippe Boullay,^[b] Gwenaëlle Rousse,^[c] Christel Gervais,^[a] Cristina Coelho Diogo,^[d] Houria Kabbour,^[e] Capucine Sassoye,^[a] Patricia Beaunier,^[f] Victor Castaing,^[g] Bruno Viana,^[g] Maria Luisa Ruiz Gonzalez,^[h,i] José Gonzalez Calbet,^[h,i] Christel Laberty-Robert,^[a] David Portehault*^[a]

[a] Dr. R. Kumar, Dr. Y. Song, A. Ghoridi, Prof. C. Gervais, Dr. C. Sassoye, Prof. C. L. Robert, Dr. D. Portehault
Sorbonne Université, CNRS, Collège de France, Laboratoire de Chimie de la Matière Condensée de Paris (CMCP), 4 place Jussieu, F-75005, Paris, France

E-mail: david.portehault@sorbonne-universite.fr

[b] Dr. P. Boullay
Normandie Université, ENSICAEN, UNICAEN, CNRS, CRISMAT, 14000 Caen, France

[c] Dr. G. Rousse
PSL Research University, Sorbonne Université, Collège de France, Chimie du Solide et de l'Energie, UMR 8260, Collège de France, 11 place Marcelin Berthelot, 75007 Paris, France

[d] Dr. C. Coelho Diogo
Sorbonne Université, CNRS, Institut des Matériaux de Paris-Centre, IMPC, F-75005, Paris, France

[e] Dr. H. Kabbour
Univ. Lille, CNRS, ENSCL, Centrale Lille, Univ. Artois, UMR 8181-UCCS-Unité de Catalyse et de Chimie du Solide, F-59000 Lille, France

[f] P. Beaunier
Sorbonne Université, CNRS, Laboratoire de Réactivité de Surface (LRS), 4 place Jussieu, F-75005, Paris, France

[g] Dr. V. Castaing, Dr. B. Viana
PSL Research University, Chimie ParisTech, CNRS, Institut de Recherche de Chimie de Paris, 11 rue Pierre et Marie Curie, 75005 Paris, France

[h] Dr. M. Luisa Ruiz Gonzalez, Prof. J. G. Calbet
Departamento de Química Inorgánica, Facultad de Químicas, Universidad Complutense, 28040-Madrid, Spain

[i] Centro Nacional de Microscopía Electrónica, Universidad Complutense, 28040 Madrid, Spain

Supporting information for this article is given via a link at the end of the document.

Abstract: Mixed-anion compounds widen the chemical space of attainable materials compared to single anionic compounds, but the exploration of their structural diversity is limited by common synthetic paths. Especially, oxychlorides rely mainly on layered structures, which suffer from low stability during photo(electro)catalytic processes. Herein we report a strategy to design a new polar 3D tetrahedral framework with composition $Zn_4Si_2O_7Cl_2$. We use a molten salt medium to enable low temperature crystallization of nanowires of this new compound, by relying on tetrahedral building units present in the melt to build the connectivity of the oxychloride. These units are combined with silicon-based connectors from a non-oxidic Zintl phase to enable precise tuning of the oxygen content. This structure brings high chemical and thermal stability, as well as strongly anisotropic hole mobility along the polar axis. These features, associated with the ability to adjust the transport properties by doping, enable to tune water splitting properties for photoelectrocatalytic H_2 evolution and water oxidation. This work then paves the way to a new family of mixed-anion solids

Introduction

Mixed-anion metal compounds contain metal cations bounded to two different anions.^[1,2] The resulting heteroleptic cation-centered polyhedra provide an additional dimension to access ionic conductivity,^[3] superconductivity,^[4] magnetic,^[5] optical^[6] and

(photo)catalytic properties^[7] that provide new horizons for batteries,^[3] nonlinear optics,^[8] water splitting^[7,9] and optoelectronics.^[10] Among these materials, metal oxyhalides are a largely uncovered territory compared to the vast library of oxides and halides because their composition space is hard to explore by conventional solid-state synthesis methods at high temperatures, where they often decompose by halogen loss.^[11] Topochemical,^[5] solvothermal^[12] and flux syntheses^[13,14] enable to decrease the reaction temperatures and to isolate original oxyhalides by accessing new reaction pathways. Yet, the structural diversity of oxyhalides remains limited. Especially, metal oxychlorides mostly rely on layered structures where metal-oxygen layers terminated with Cl^- ions interact together by van der Waals interactions that render chloride ions particularly labile.^[5,6,15–17] Stability is further undermined by the prominent contribution of Cl 3p states at the top of the valence band, which makes them prone to photocorrosion, apart some Bi-based materials.^[14,18] Besides stability considerations, aiming at oxychlorides with 3D structures instead of layered ones can yield new phenomena, like spin-induced high- T_c multiferroicity.^[19]

Herein, we present a reaction pathway towards a chemically and thermally stable metal oxychloride based on a new polar 3D tetrahedral framework (**Figure 1**). This material shows strongly anisotropic hole mobility along the polar axis and photoelectrocatalytic activity for H_2 production from water.

To explore how 3D connectivity can yield new oxychlorides, we design a reaction path by following 3 principles. First, we use

RESEARCH ARTICLE

molten salts media at lower temperature (420 °C) than usual flux syntheses of oxyhalides,^[13,14] to avoid thermal decomposition of the product during synthesis, while enabling the recovery of metastable solids.^[20] As liquid media, molten salts also increase the nucleation and crystallization rates compared to solid-state reactions,^[21] thus giving access to nano-objects,^[21] which are scarce among oxyhalides and exacerbate the impact of the surface on the properties, especially for catalysis. Second, we use $[\text{SiO}_4]$ tetrahedral connectors already observed in the few metal-silicon oxyhalides reported (27 entries in the Inorganic Crystal Structure Database excluding Rare Earths),^[17] especially in $\text{Cd}_4\text{Si}_2\text{O}_7\text{F}_2$,^[22] which has been the only oxyhalide of silicon and a post-transition metal before the present work.^[17] As metal cation, we focus on Zn^{2+} because its parent ZnO and ZnCl_2 structures are also built on tetrahedral units, and compounds of d^{10} metal cations are of interest for photocatalysis.^[23] Zinc has never been reported in a non-hydrated, thermally stable oxychloride compound.^[24,25] We anticipate that $[\text{SiO}_4]$ connectors could bridge Zn units through Si-O-Zn bonds by reacting with $[\text{ZnCl}_4]$ tetrahedra. Molten salts based on ZnCl_2 have actually been described as polymeric liquids made of interconnected $[\text{ZnCl}_4]$ tetrahedra,^[26] so that the structure of the solid could be directly related to the liquid structure by using such salts. Third, in order to control independently the Si/Zn ratio and O stoichiometry, we use a specific oxygen-free silicon

precursor: sodium silicide Na_4Si_4 (Figure S1). This Zintl solid is simpler to handle than most silanes and silicon halides^[27] and is usually employed to produce non-oxide materials, including Si allotropes, clathrates and nanoscaled metal silicides.^[28–30] It contains $[\text{Si}_4]^{4-}$ clusters that are readily oxidized by oxygenated species. Its reactivity has not been explored to yield oxo-species with controlled oxygen content. This combination of Zn and Si into an oxychloride framework could deliver a new Earth-abundant photocatalyst

Results and Discussion

We choose the eutectic molten salt medium $\text{ZnCl}_2:\text{NaCl}$ (68:32 mol., melting point = 260 °C) to enable a wide temperature range in the liquid state (see detailed procedure in Supplementary information SI). Oxygen is provided in a small proportion either by using $\text{ZnCl}_2 \cdot 1.33\text{H}_2\text{O}$ impurities in commercial ZnCl_2 (overall Si/Zn, O/Si and O/Zn molar ratios are 0.05, 2.4 and 0.13, respectively, according to thermogravimetric analysis (TGA, Figure S2 in SI)), or by using anhydrous ZnCl_2 (99.999%) with addition of a small amount of water ($\text{H}_2\text{O}/\text{ZnCl}_2$ mol. ratio 0.415).

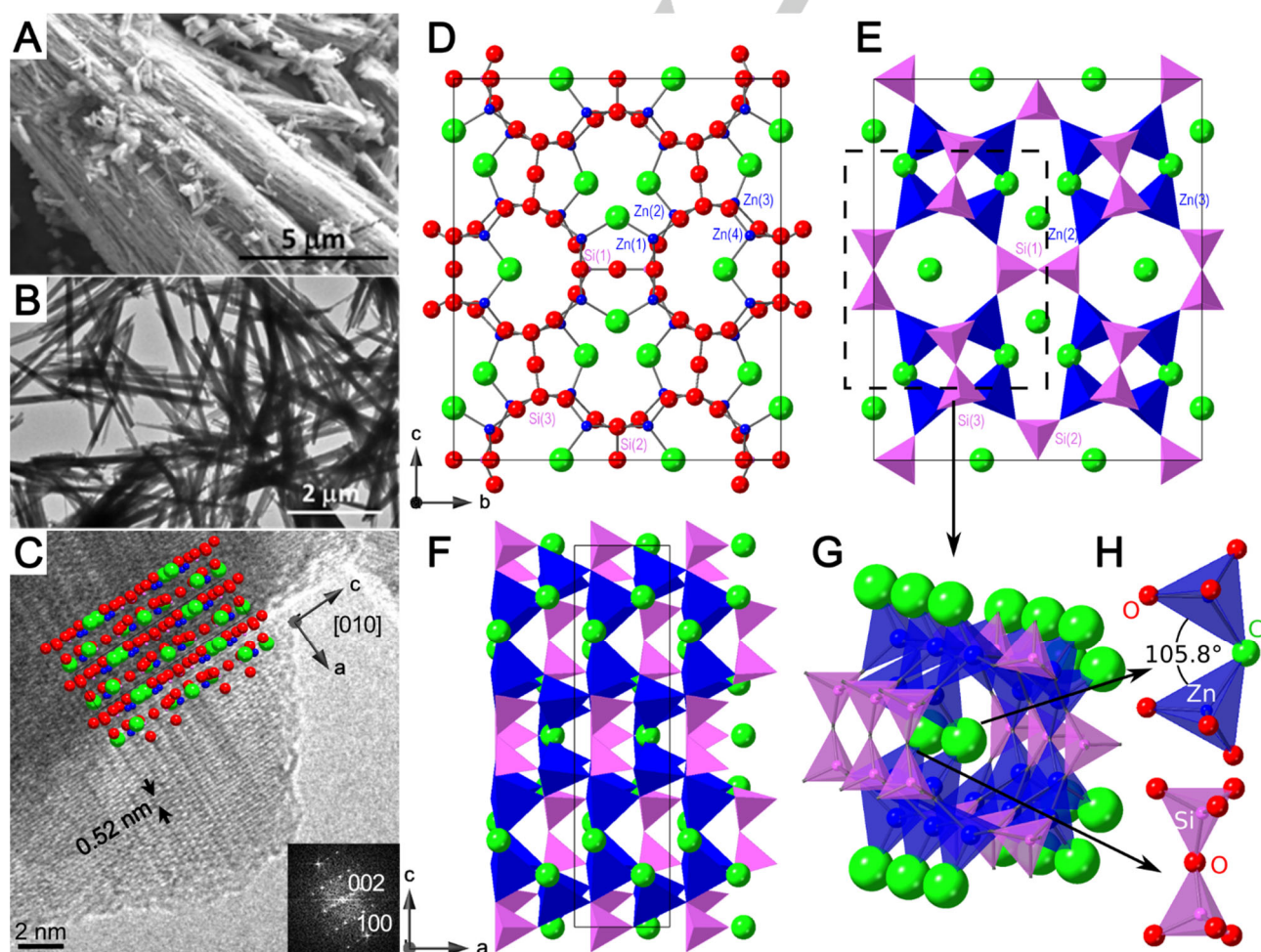


Figure 1. Nanoscale and atom-scale structure of $\text{Zn}_4\text{Si}_2\text{O}_7\text{Cl}_2$. (A, B) SEM and TEM images of $\text{Zn}_4\text{Si}_2\text{O}_7\text{Cl}_2$ nanowires. (C) HRTEM image along the $[010]$ zone axis and corresponding atomic arrangement (Cl = green, O = red, Zn = blue, Si = yellow) derived from electron diffraction and XRD. Atomic (D) and (E) polyhedral representations of the $[001]$ projection of $\text{Zn}_4\text{Si}_2\text{O}_7\text{Cl}_2$ structure (ZnO₃Cl tetrahedra = blue, SiO₄ tetrahedra = purple, Cl = green). (F) Polyhedral representation along $[010]$. (G) 1D-tunnel along the $[100]$ direction. (H) Cl-bridged ZnO₃Cl and SiO₄ tetrahedra dimers as building blocks of the structure.

RESEARCH ARTICLE

After washing of the salts, the reaction performed at 420 °C yields a grey powder made of high aspect ratio nanowires with 20 to 50 nm diameter and hundreds of nanometers to micrometers length (Figures 1A-B, S3 and S4), with a Brunauer-Emmett-Teller (BET) surface area of 17 m² g⁻¹. Energy dispersive X-ray spectroscopy (EDS) indicates a Zn:Si:Cl composition of 4:2:2 (Figure S5). Scanning transmission electron microscopy (STEM)-High-angle annular dark field (HAADF) imaging and STEM-EDS elemental mapping (Figure S6) show the homogeneous distribution of Zn, Si, O and Cl. The nanowires were already detected within the salt medium, before washing (Figure S7).

The powder X-ray diffraction (XRD) pattern could not be indexed along any structure reported. Increasing the reaction time up to 100 h or thermally annealing the powders only resulted in an increase of the nanowires length and did not deliver bulk single crystals (Figure S8). The small size of the nanowires was detrimental to the deconvolution of XRD peaks for precise assessment of their relative intensities, thus precluding identification of any structural model. To overcome this limitation, structure analysis was carried out by precession-assisted electron diffraction tomography (PEDT), a 3D single crystal electron diffraction technique^[31] enabling to solve the structure of materials with sub-micrometer size (see detailed description of PEDT and XRD results in supplementary information S-5 and S-10). Despite diffuse scattering (Figure S9) indicating structural disorder, the reconstructed reciprocal space enabled to retain a A-centered orthorhombic lattice with unit cell parameters $a \approx 5.2$ Å, $b \approx 17.5$ Å and $c \approx 20.7$ Å. *Ab initio* structure solution by the charge flipping method^[32] was performed from the data acquired on two nanowires for high completeness of the data set (Table S1). According to symmetry analysis,^[33] the polar $A2mm$ group was retained with a structure encompassing 21 independent atoms revealed from the electrostatic potential map (Figure S10). This

structural model was refined (Tables S2 and S3) with the stoichiometry Zn₄Si₂O₇Cl₂ by considering dynamical diffraction effects.^[34] This new structure is fully supported by calculations of interatomic distances and bond valence strengths (Table S4). One can identify ZnO₃Cl tetrahedra bridged by Cl atoms (Figure 1D-H). (ZnO₃)₂Cl dimers are bridged by dimers of corner-sharing [SiO₄] tetrahedra. The polar axis is the *a* axis along which all tetrahedra apexes are oriented (Figure 1F). This axis also corresponds to the channels delimited alternatively by 7 tetrahedra (4Zn+3Si) and 6 tetrahedra (4Zn+2Si). In the latter case, one chlorine atom points towards the center of the channels. A Rietveld analysis conducted on a synchrotron powder XRD (SXRD) pattern of the whole powder (Figure 2A, Table S5) confirms the structural model issued from PEDT on only a few nanowires. Analysis of the anisotropic size broadening of the SXRD peaks yields reconstructed needle-like crystallites grown along the [100] direction (Figure 2A), in full agreement with electron microscopy (Figures 1 and S11).

Zn₄Si₂O₇Cl₂ is one of the rare solids and the first metal oxyhalide crystallizing in the polar $A2mm$ space group (Table S6). It is also the only one built only from coordination tetrahedra. This 3D interconnected framework obviously deviates from the trend of oxychlorides to grow 2D structures.

The crystal structure of this new compound is confirmed by ²⁹Si MAS solid-state nuclear magnetic resonance NMR (Figure 2B) with two main signals typical of SiO₄ tetrahedra at approx. -70 and -81 ppm in a 20:80 ratio, which are ascribed to Si(3) on one hand, Si(1) and Si(2) on the other hand according to density functional theory DFT calculations (Figure 2B, S-8). The static ³⁵Cl solid-state NMR spectrum is also reasonably fitted with the DFT calculated parameters of the 3 chlorine positions (Figure S12). Electron energy loss spectroscopy (EELS) highlights Si-L_{2,3} and Si-L₁ edges (Figure 2C) at ca. 100 and 150 eV, which are characteristic of Si⁴⁺ in tetrahedra

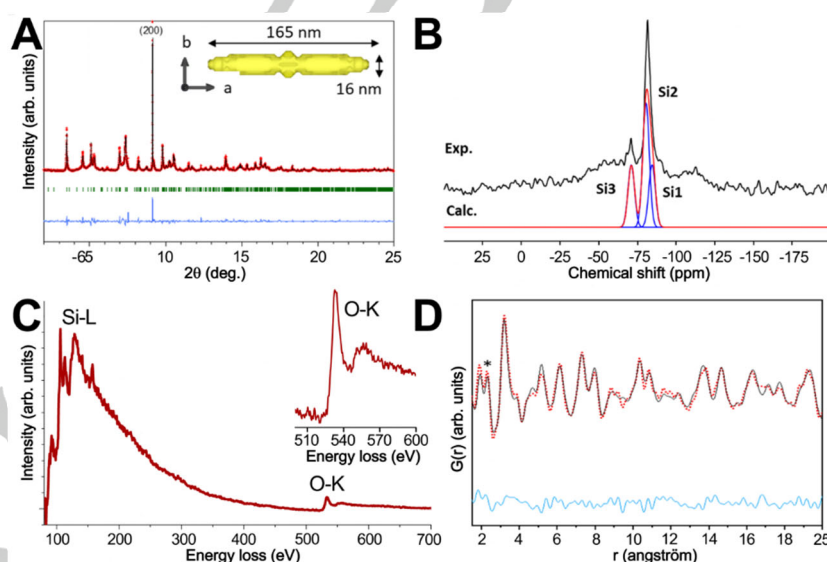


Figure 2. X-ray diffraction, scattering and spectroscopic evidences of the Zn₄Si₂O₇Cl₂ structure. (A) Rietveld refinement of the SXRD pattern of Zn₄Si₂O₇Cl₂ ($\lambda = 0.412831$ Å). The red crosses, black, and blue lines, and green tick bars represent the observed, calculated, and difference patterns, and Bragg positions, respectively. As inset is the crystallite shape deduced from the refinement of the anisotropic size broadening. (B) Experimental ²⁹Si MAS solid-state NMR spectrum of the Zn₄Si₂O₇Cl₂ nanowires and the corresponding spectrum calculated by DFT with the structure from refined PEDT data. (C) EELS spectrum showing the characteristic Si-L and O-K edges, respectively (Inset: enlarged view of O-K edge). (D) Pair distribution function (PDF) analysis of the nanowires (experimental = red, fitting = black, difference = blue) taking into account the presence of amorphous silicon (*).

RESEARCH ARTICLE

coordination SiO_4^{2-} .^[35] The O-K edge at 533 eV is typical of O^{2-} species. The Zn L_3 , L_2 and L_1 edges are also typical of Zn^{2+} oxo species at 1021, 1044 and 1194 eV (Figure S13), respectively.^[35] X-ray photoelectron spectroscopy (XPS, Figure S14 and Table S7) and Fourier Transform Infrared spectroscopy (Figure S15) are consistent with Zn^{2+} and Si^{4+}O_4 units as well as with Zn-Cl bonds.

The ^{29}Si NMR spectrum (Figure 2B) exhibits a wide and low intensity signal below the narrow signals assigned to crystalline $\text{Zn}_4\text{Si}_2\text{O}_7\text{Cl}_2$. This feature could correspond to an amorphous component. Hence, before addressing photoelectronic properties, we have analyzed the total X-Ray scattering pattern with the Pair Distribution Function (PDF) to assess the presence of non-crystalline solids (Figure 2D).^[36–38] The PDF refinement of the experimental $G(r)$ curve is fully consistent with the PEDT crystal structure (Figure 2D, reliability factor $R_w = 28.1\%$). An additional correlation distance is found at 2.30 Å and attributed to amorphous silicon impurities, as shown by the improved reliability factor when amorphous Si is considered ($R_w = 23.8\%$, Figure S16). This component then accounts for the wide and weak signal observed on the ^{29}Si NMR spectrum. We ascribe this amorphous Si component to the side-decomposition of Na_4Si_4 . The $\text{Si}^0/\text{Si}^{4+}$ ratio is 0.05 according to XPS, which corresponds to ~ 0.6 wt.% of amorphous silicon (Figure S17).

The $\text{Zn}_4\text{Si}_2\text{O}_7\text{Cl}_2$ structure is built from SiO_4 and ZnO_3Cl tetrahedral building blocks that can be traced back to the reaction mixture. Indeed, while $[\text{SiO}_4]$ units are readily formed by the oxidation of Na_4Si_4 by small amounts of water, Zn-based units originate from molten ZnCl_2 , which is a polymeric liquid made of ZnCl_4 tetrahedra linked together by corners and edges.^[26] Mixing ZnCl_2 with NaCl brings Na^+ ions that partially break the tetrahedra network^[39] and yield small clusters of ZnCl_4 tetrahedra where zinc cations are linked by chloride ions, especially $(\text{Cl}_3\text{Zn})\text{Cl}(\text{ZnCl}_3)$ dimers where the 6 Cl terminating groups can react with $[\text{SiO}_4]$ building blocks for growing a zinc oxychloride framework. Note that using water-free zinc chloride (99.999% purity) without incorporation of water results in metallic zinc as the major crystalline phase, which originates from the reduction of ZnCl_2 by Na_4Si_4 in the absence of oxygen and water.

Thermogravimetric analysis (Figure S18) shows the high thermal stability in air or nitrogen of $\text{Zn}_4\text{Si}_2\text{O}_7\text{Cl}_2$, which decomposed at 600 °C into ZnO and silica by chlorine loss. In the title compound, Cl is locked by bridging two ZnO_3Cl tetrahedra within structural channels, which ensures enhanced thermal stability than layered metal oxychlorides, where Cl is located between the metal-oxo layers weakly bonded to each other, with resulting lower temperature of chlorine loss and decomposition (~ 450 °C).^[40] No thermal degradation is observed on annealing at 500 °C under argon for one week or air for one day (Figure S19). Further, the nanowires show no degradation after dispersion (Figure S20) for one year in water or methanol and high stability in alkaline and mildly acidic (pH 4) conditions, although the compound decomposes in more acidic medium.

Upon UV excitation at room temperature, we observed a strong blue emission (Figure 3A), with an emission band centered at about 2.8 eV (450 nm). A shoulder around 3.4 eV (370 nm) clearly detected at low temperature is ascribed to band-to-band relaxation in $\text{Zn}_4\text{Si}_2\text{O}_7\text{Cl}_2$ and is indicative of the band gap. The 450 nm broad emission band is assigned to recombination through Si-related shallow defect centers.^[41,42] Such defects induce long lifetimes,^[42] as observed for the 2.8 eV emission

(450 nm, Figure S21) with a lifetime value of about 12 μs . UV-visible diffuse reflectance measurements (Figure 3B) indicate a band gap of 3.3 eV. DFT calculations were used to get deeper insights into the electronic structure. A full geometry relaxation (Table S8) yields little changes in the experimentally determined structural parameters. The band structure (zoom in Figure 3C and overall view in Figure S22) indicates a direct band gap of 3.3 eV consistent with diffuse reflectance.

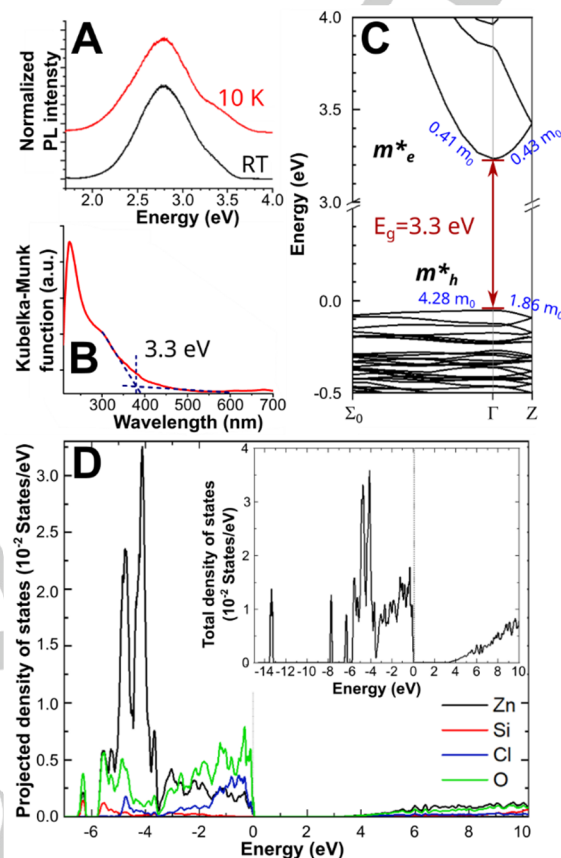


Figure 3. Optical and electronic properties. (A) Emission spectra at 10 K and room temperature. (B) Kubelka-Munk function obtained from UV-visible diffuse reflectance measurements. (C) Zoom in the band structure of $\text{Zn}_4\text{Si}_2\text{O}_7\text{Cl}_2$ with the valence band maximum (VBM) and conduction band minimum (CBM) highlighted and showing a direct band gap of 3.28 eV at the Γ point. The effective masses of electrons and holes calculated along the different directions are indicated. (D) Projected Density of States (PDOS) for $\text{Zn}_4\text{Si}_2\text{O}_7\text{Cl}_2$ on each type of element within the unit cell. The inset represents the total DOS. The Fermi level is set to 0 eV.

To investigate the role of the structure polarity on charge transport, we have calculated the effective mass of the charge carriers (Table S9). The effective mass of electrons (m_e^*) is isotropic. Its low value of $\sim 0.4 m_0$ highlights the high mobility of photo-generated electrons. It is one order of magnitude lower than for holes (m_h^*) (Figure 3C), which then promotes the separation of photoinduced electron-hole pairs. The DFT-calculated dipole moment of the unit cell is oriented along the polar [100] direction and exhibits a high value of 16.5 e Å, thus yielding a strong built-in electric field along the polar axis.^[43,44] The polarity of the structure is also linked to the pronounced acentric character of the heteroleptic tetrahedral units ZnO_3Cl . m_h^* shows a strong anisotropy (Table S9) with the smallest values along the [100] direction, parallel to the dipole moment. The built-in electric field

RESEARCH ARTICLE

is then along the direction of the easiest hole migration, which further enhances the separation of charge carriers and the photoelectrocatalytic activity.^[23,45] The total density of states (DOS) and projected DOS (PDOS) are shown in **Figure 3D** with additional orbital resolved PDOS in **Figure S23** focusing on the heteroleptic unit ZnO_3Cl . The dispersive conduction band encompasses contributions of all elements, in particular Zn s and p states at the conduction band minimum (CBM). The valence band (VB) consists mainly in O 2p and Cl 3p orbitals hybridized with Zn states (**Figure 3F**). Si states are found lower in the VB. Most of the Cl contribution is at the top of the VB from just below the Fermi level to about -6 eV with a major contribution centered around -1 eV. O states are found in a larger range from -8 to 0 eV, in the same region and even at slightly higher energy than Cl, contrary to what would be expected given the lower electronegativity of Cl compared to O and the knowledge on previous oxyhalides.^[14,18] This situation is beneficial for stability in water and photocatalytic water splitting since O states at the VB maximum (VBM) restrain oxidation of the halide anion and then stabilize the material *versus* self-decomposition.^[18] According to Mulliken electronegativities,^[46,47] the band edges should encompass the redox potentials of water couples.

We then assessed the possibility of doping the framework. The synthesis was performed in a glassy carbon crucible and yielded a powder with identical XRD pattern (**Figure S24**) and dark color. XPS (**Figure S25**) indicates an additional contribution to the C1s signal at 283 eV, which is attributed to a carbide environment.^[48] This XPS component accounts for a carbon/zinc elemental ratio of 0.1. The band structure of this doped material was further studied by electrochemical impedance spectroscopy. A Mott-Schottky plot (**Figure 4A**) recorded at pH 7.4 exhibits a positive slope, indicating an n-type semiconductor behavior for C-doped $\text{Zn}_4\text{Si}_2\text{O}_7\text{Cl}_2$. From this plot, the flat band potential E_{FB} is evaluated at -0.12 V vs. The reversible hydrogen electrode (RHE, pH = 7.4) (**Figure 4A**). With a difference of 0.2 V between E_{FB} and the CBM in a n-type semiconductor,^[49] the CBM lies at ca. -0.3 V

vs. RHE (**Figure 4B**). By taking into account the band gap of 3.3 eV, the VBM is located at 3.0 V vs. RHE at pH 7.4.

Undoped $\text{Zn}_4\text{Si}_2\text{O}_7\text{Cl}_2$ yielded scattered Mott-Schottky data (not shown), which can be related to poorer conductivity than for the carbon-doped material. We then measured the flat band potential at different pH values in the stability range of the material by linear sweep voltammetry under chopped illumination. This method is usually more reliable than the Mott-Schottky method.^[50] The amplitude of the anodic and cathodic currents are comparable (**Figure S26A**), which is characteristic of an ambipolar behavior of the semiconductor. E_{FB} decreases linearly with increasing pH values (**Figure S26B**), with a slope of 23 mV pH^{-1} , which deviates from the Nernstian behavior met in oxides, as observed for semiconductor oxides and other oxyhalides,^[51] which could be related to different free energies of proton adsorption and desorption.^[52] E_{FB} at pH 7.4 is evaluated at 0.7 V vs. RHE, respectively. As an estimation of the CBM and VBM positions, we follow the indication of ambipolarity to state that the flat band potential is in the middle of the band gap. With this assumption, the CBM and VBM positions are reasonably consistent with those evaluated for C-doped $\text{Zn}_4\text{Si}_2\text{O}_7\text{Cl}_2$ and with calculations based on Mulliken electronegativities.^[46,47] This confirms that C-doping does not modify in depth the band structure and that the band positions are suitable for water splitting near neutral pH for undoped and C-doped $\text{Zn}_4\text{Si}_2\text{O}_7\text{Cl}_2$.

Overall, $\text{Zn}_4\text{Si}_2\text{O}_7\text{Cl}_2$ is a semiconductor that combines adequate VB and CB positioning *versus* water oxidation/reduction half-reactions, long term stability in water, mobility of charge carriers, ability to efficiently separate charge carriers thanks to very different carrier mobilities and to a strong built-in electric field^[44] linked to the polarity of the structure and the particle anisotropy. These features are promising for photoelectrochemical (PEC) water splitting and add to the recent interest of heteroleptic environments for water-splitting.^[14,53,54] Although oxyhalides show promises in the photocatalytic degradation of organic dyes and water splitting,^[14,55,56] very little

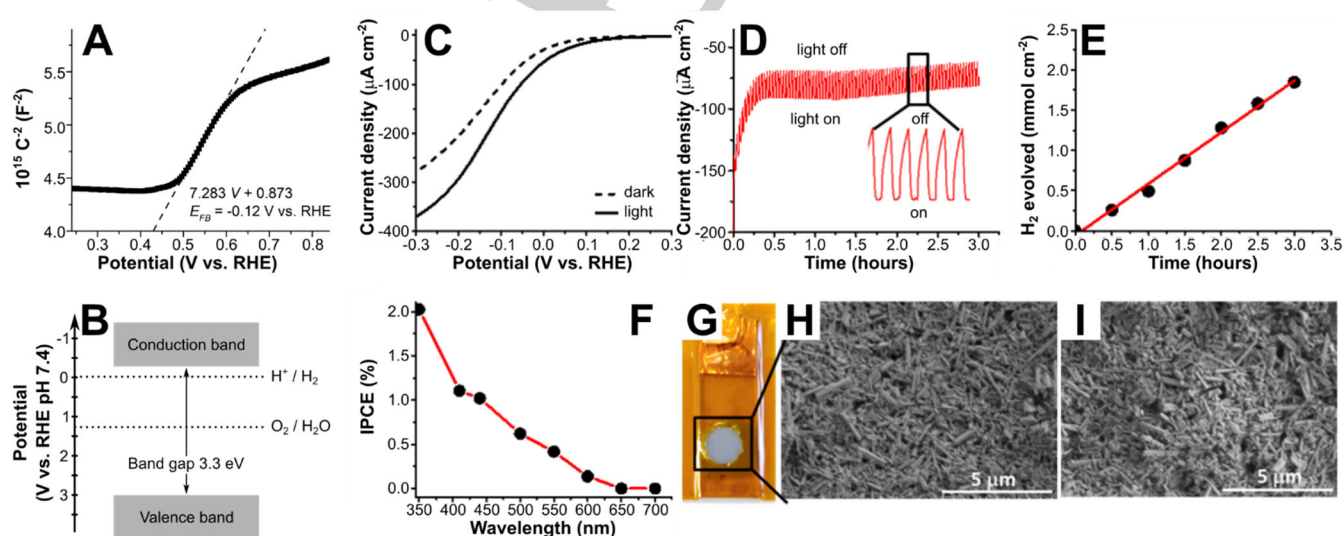


Figure 4. Photoelectrocatalytic water splitting with $\text{Zn}_4\text{Si}_2\text{O}_7\text{Cl}_2$ nanowires. (A) Mott-Schottky plot recorded at 100 kHz in a 0.1 M Na_2SO_4 electrolyte at pH 7.4. (B) Scheme of the band structure versus potentials of water redox couples at pH 7.4. (C) Linear sweep voltammetry of a $\text{Zn}_4\text{Si}_2\text{O}_7\text{Cl}_2$ photoelectrode at a scan rate of 10 mV s^{-1} in 0.1 M Na_2SO_4 . (D) Chopped-light chronoamperometric measurement of a $\text{Zn}_4\text{Si}_2\text{O}_7\text{Cl}_2$ photoelectrode biased at -0.05 V/RHE (shutter time = 1 min for each plateau, 0.1 M Na_2SO_4 , 280 W Xe-lamp). (E) Electrode surface normalized evolution of H_2 vs. time at a bias of -0.2 V/RHE (0.1 M Na_2SO_4 , 280 W Xe-lamp). (F) Incident photon to current conversion efficiency (IPCE) of $\text{Zn}_4\text{Si}_2\text{O}_7\text{Cl}_2$ nanowires biased at -0.2 V/RHE and under different monochromatic wavelengths in 0.1 M Na_2SO_4 . (G) Photoelectrode used in water splitting experiments. (H) Top-view SEM images of the electrode before and (I) after the H_2 evolution experiment.

RESEARCH ARTICLE

has been reported on their PEC properties. As an ambipolar material, undoped $\text{Zn}_4\text{Si}_2\text{O}_7\text{Cl}_2$ may operate in both water reduction and oxidation half-reactions. We focused on the H_2 evolution cathodic side, for which efficient oxide-based materials are scarce. Photoelectrochemical measurements were then performed in a 0.1 M Na_2SO_4 electrolyte under a 280W Xenon lamp (Figure 4C). Linear sweep voltammetry (LSV) for the undoped material shows larger cathodic current under light, in agreement with photocatalytic reduction of water. Chronoamperometry at a bias of -0.05 V/RHE show a decrease in the cathodic current over the first 0.5 h, which cannot be related to any structural evolution, as EDS, XRD, scanning electron microscopy (SEM) and TEM (Figures 4G-I and S27, S28) confirm the excellent stability of the nanowires with no compositional, morphological or structural evolution after H_2 evolution. After 0.5 h, the photocurrent reaches a steady state with no significant decrease even after several hours under chopped on/off light (Figure 4D). The photocurrent is $23 \pm 0.7 \mu\text{A cm}^{-2}$ under light during chronoamperometry evaluated from three measurements. Water photoelectrolysis at a bias of -0.2 V vs RHE (Figure 4E) for three hours under the Xe lamp results in the evolution of $3.7 \mu\text{mol}$ (or $1.85 \mu\text{mol cm}^{-2}_{\text{electrode}}$) of H_2 quantified by gas chromatography, thus corresponding to a Faradaic efficiency of $(85 \pm 14)\%$ (Figures 4C, S30). The incident photon-to-current conversion efficiency (IPCE) measured at different monochromatic wavelengths in visible–UV region shows highest conversion efficiency of ca. 2% at 350 nm (Figure 4F), in agreement with the 3.3 eV band gap and diffuse reflectance UV-visible spectroscopy (Figure 3B).

C-doped $\text{Zn}_4\text{Si}_2\text{O}_7\text{Cl}_2$ shows the behavior expected for an n-type semiconductor: enhanced activity in the anodic range for oxygen evolution (Figures S30 and S31). The ability to tune the semiconductor type by doping in oxychlorides brings further opportunities to tune electrochemical and transport properties in the future.

Conclusions

We have described the first zinc-silicon oxyhalide, $\text{Zn}_4\text{Si}_2\text{O}_7\text{Cl}_2$ as high aspect ratio nanowires. It crystallizes in a unique polar structure built on tetrahedral units that originate from the molten salt reaction medium. This 3D framework stands out from common layered metal oxychlorides, by providing high thermal and chemical stability. The ambipolar behavior we detected and the strong electric field built in the polar structure provides suitable conditions for photoelectrochemical H_2 production from water. Our synthesis approach relies on a low valence non oxidic silicon precursor and on molten salts as liquid reaction media and reagents. This method allows triggering the crystallization of complex compounds at low temperature and then isolating metastable solids, which would be prone to decomposition in harsher conditions. We demonstrate that the approach is suitable for controlled doping and then adjustment of the nature of major charge carriers. This last result emphasizes our ability to extensively tune the composition and electronic structure of oxyhalides by synthesis in molten salts. This paves the way to an entirely new family of mixed anion solids.

Supplementary Information

Methods details, Figures S1 to S31 and Tables S1 to S9 for structural, chemical and electrochemical characterization studies. Crystallographic Information File from PEDT refinement, corresponding CheckCIF report. Crystal structure details can be found in the Cambridge Crystallographic Data Centre under the depository number 2073127.^[67]

Acknowledgements

The authors acknowledge the CNRS and Collège de France for funding. This project has received funding from the European Research Council (ERC) Consolidator Grant GENESIS under the European Union's Horizon 2020 research and innovation programme (grant agreement n° 864850). PEDT experiments were performed on the IRMA platform (CRISMAT-Caen) of the CNRS-CEA METSA network (FR CNRS 3507). XPS and some TEM, STEM-EDS experiments were performed using the facilities of Institut des Matériaux de Paris Centre (Sorbonne Université). This work used resources of the Advanced Photon Source (11-BM), a U.S. Department of Energy (DOE) Office of Science User Facility operated for the DOE Office of Science by Argonne National Laboratory under Contract No. DE-AC02-06CH11357. NMR spectroscopic calculations were performed using HPC resources from GENCI-IDRIS (Grant 097535). The French Région Ile de France - SESAME program is also acknowledged for financial support (700 MHz NMR spectrometer).

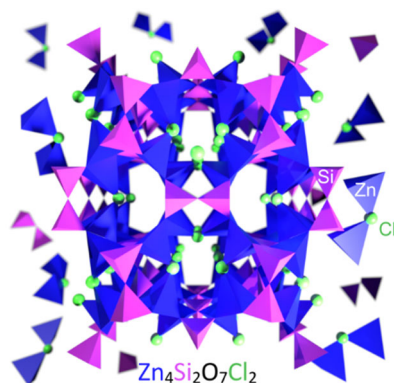
Keywords: mixed anions, oxychloride, molten salts, electron crystallography, photoelectrocatalysis.

- [1] H. Kageyama, K. Hayashi, K. Maeda, J. P. Atfield, Z. Hiroi, J. M. Rondinelli, K. R. Poeppelmeier, *Nat. Commun.* **2018**, *9*, 772.
- [2] J. K. Harada, N. Charles, K. R. Poeppelmeier, J. M. Rondinelli, *Adv. Mater.* **2019**, *31*, 1805295.
- [3] N. Imanaka, K. Okamoto, G. Adachi, *Angew. Chem. Int. Ed.* **2002**, *41*, 3890.
- [4] M. Ai-Mamouri, P. P. Edwards, C. Greaves, M. Slaski, *Nature* **1994**, *369*, 382.
- [5] L. Viciu, J. Koenig, L. Spinu, W. L. Zhou, J. B. Wiley, *Chem. Mater.* **2003**, *15*, 1480.
- [6] J. Olchowka, H. Kabbour, M. Colmont, M. Adlung, C. Wickleder, O. Mentré, *Inorg. Chem.* **2016**, *55*, 7582.
- [7] R. Kuriki, T. Ichibha, K. Hongo, D. Lu, R. Maezono, H. Kageyama, O. Ishitani, K. Oka, K. Maeda, *J. Am. Chem. Soc.* **2018**, *140*, 6648.
- [8] Y.-Y. Li, W.-J. Wang, H. Wang, H. Lin, L.-M. Wu, *Cryst. Growth Des.* **2019**, *19*, 4172.
- [9] K. Lemoine, J. Lhoste, A. Hémon-Ribaud, N. Heidary, V. Maisonneuve, A. Guet, N. Kornienko, *Chem. Sci.* **2019**, *10*, 9209.
- [10] H. Shi, W. Ming, M.-H. Du, *Phys. Rev. B* **2016**, *93*, 104108.
- [11] X. Tao, Y. Zhao, L. Mu, S. Wang, R. Li, C. Li, *Adv. Ener. Mater.* **2018**, *8*, 1701392.
- [12] A. Tressaud, K. R. Poeppelmeier, Eds., *Photonic and Electronic Properties of Fluoride Materials: Progress in Fluorine Science Series*, Elsevier, Amsterdam, **2016**.
- [13] D. Carone, V. V. Klepov, M. D. Smith, H. C. Zur Loye, *Inorg. Chem.* **2019**, *58*, 16831.
- [14] K. Chatterjee, R. Dos Reis, J. K. Harada, J. K. Mathiesen, S. L. A. Bueno, K. M. Ø. Jensen, J. M. Rondinelli, V. David, S. E. Skrabalak, *Chem. Mater.* **2021**, *33*, 347.
- [15] D. H. Templeton, C. H. Dauben, *J. Am. Chem. Soc.* **1953**, *75*, 6069.
- [16] A. Nakada, M. Higashi, T. Kimura, H. Suzuki, D. Kato, H. Okajima, T. Yamamoto, A. Saeki, H. Kageyama, R. Abe, *Chem. Mater.* **2019**, *31*, 3419.

RESEARCH ARTICLE

- [17] NIST Inorganic Crystal Structure Database, NIST Standard Reference Database Number 3, National Institute of Standards and Technology, Gaithersburg MD, 20899, DOI: <https://doi.org/10.18434/M32147>, (retrieved 2023/02/22).
- [18] D. Kato, K. Hongo, R. Maezono, M. Higashi, H. Kunioku, M. Yabuuchi, H. Suzuki, H. Okajima, C. Zhong, K. Nakano, R. Abe, H. Kageyama, *J. Am. Chem. Soc.* **2017**, *139*, 18725–18731.
- [19] L. Zhao, M. T. Fernández-Díaz, L. H. Tjeng, A. C. Komarek, *Sci. Adv.* **2016**, *2*, e1600353.
- [20] X. Zhou, V. S. C. Kolluru, W. Xu, L. Wang, T. Chang, Y. S. Chen, L. Yu, J. Wen, M. K. Y. Chan, D. Y. Chung, M. G. Kanatzidis, *Nature* **2022**, *612*, 72.
- [21] D. Portehault, I. Gómez-Recio, M. A. Baron, V. Musumeci, C. Aymonier, V. Rouchon, Y. Le Godec, *Chem. Soc. Rev.* **2022**, *51*, 4828.
- [22] S. N. Achary, A. K. Tyagi, M. K. Gupta, R. Mittal, K. Bhattacharya, R. Rao, *J Alloys Comp.* **2017**, *702*, 573.
- [23] S. Nishioka, T. Kanazawa, K. Shibata, Y. Tsujimoto, H. C. Zur Loye, K. Maeda, *Dalton Trans.* **2019**, *48*, 15778.
- [24] X. Wang, J. Li, G. K. Das, S. Johanie, C. Vernon, R. Shaw, *J. Solid State Chem.* **2020**, *290*, 121483.
- [25] F. C. Hawthorne, E. Sokolova, *Can. Miner.* **2002**, *40*, 939.
- [26] A. Q. Alsayoud, M. Venkateswara Rao, A. N. Edwards, P. A. Deymier, K. Muralidharan, B. G. Potter, K. Runge, P. Lucas, *J. Phys. Chem. B* **2016**, *120*, 4174.
- [27] D. Mayeri, B. L. Phillips, M. P. Augustine, S. M. Kauzlarich, *Chem. Mater.* **2001**, *13*, 765.
- [28] P. Simon, Z. Tang, W. Carrillo-Cabrera, K. Chiong, B. Böhme, M. Baitinger, H. Lichte, Y. Grin, A. M. Guloy, *J. Am. Chem. Soc.* **2011**, *133*, 7596.
- [29] L. Krishna, L. L. Baranowski, A. D. Martinez, C. A. Koh, P. C. Taylor, A. C. Tamboli, E. S. Toberer, *CrystEngComm* **2014**, *16*, 3940.
- [30] R. Kumar, M. Bahri, Y. Song, F. Gonell, C. Thomas, O. Ersen, C. Sanchez, C. Laberty-Robert, D. Portehault, *Nanoscale* **2020**, *12*, 15209.
- [31] M. Gemmi, E. Mugnaioli, T. E. Gorelik, U. Kolb, L. Palatinus, P. Boullay, S. Hovmöller, J. P. Abrahams, *ACS Cent. Sci.* **2019**, *5*, 1315.
- [32] L. Palatinus, G. Chapuis, *J. Appl. Crystallogr.* **2007**, *40*, 786.
- [33] L. Palatinus, A. Van Der Lee, *J. Appl. Crystallogr.* **2008**, *41*, 975.
- [34] L. Palatinus, C. A. Corrêa, G. Steciuk, D. Jacob, P. Roussel, P. Boullay, M. Klementová, M. Gemmi, J. Kopeček, M. C. Domeneghetti, F. Cámara, V. Petříček, *Acta Cryst. B Struct. Sci. Cryst. Eng. Mater.* **2015**, *71*, 740.
- [35] C. C. Ahn, O. L. Krivanek, R. P. Burgner, M. M. Disko, P. R. Swann, *EELS Atlas: A Reference Collection of Electron Energy Loss Spectra Covering All Stable Elements*, Gatan, Warrendale, PA, **1983**.
- [36] S. J. L. Billinge, M. G. Kanatzidis, *Chem. Commun.* **2004**, *4*, 749.
- [37] O. Masson, P. Thomas, *J. Appl. Crystallogr.* **2013**, *46*, 461.
- [38] P. Juhás, T. Davis, C. L. Farrow, S. J. L. Billinge, *J. Appl. Crystallogr.* **2013**, *46*, 560.
- [39] V. R. Manga, N. Swintek, S. Bringuier, P. Lucas, P. Deymier, K. Muralidharan, *J. Chem. Phys.* **2016**, *144*, 094501.
- [40] J.-M. Song, C.-J. Mao, H.-L. Niu, Y.-H. Shen, S.-Y. Zhang, *CrystEngComm* **2010**, *12*, 3875.
- [41] Z. Lin, Y. Guo, J. Song, Y. Zhang, C. Song, X. Wang, R. Huang, *J. Non Cryst. Solids* **2015**, *428*, 184.
- [42] M. Lamprecht, C. Grund, B. Neuschl, K. Thonke, Z. Bryan, R. Collazo, Z. Sitar, *J. Appl. Phys.* **2016**, *119*, 155701.
- [43] M. Li, Y. Dai, X. Ma, Z. Li, B. Huang, *Phys. Chem. Chem. Phys.* **2015**, *17*, 17710.
- [44] Y. Mi, M. Zhou, L. Wen, H. Zhao, Y. Lei, *Dalton Trans.* **2014**, *43*, 9549.
- [45] Z. Lou, P. Wang, B. Huang, Y. Dai, X. Qin, X. Zhang, Z. Wang, Y. Liu, *ChemPhotoChem* **2017**, *1*, 136.
- [46] M. A. Butler, D. S. Ginley, *J. Electrochem. Soc.* **1978**, *125*, 228.
- [47] Y. Xu, M. A. A. Schoonen, *Am. Miner.* **2000**, *85*, 543.
- [48] L. M. Schoop, F. Pielhofer, B. V. Lotsch, *Chem. Mater.* **2018**, *30*, 3155.
- [49] Y. Matsumoto, *J. Solid State Chem.* **1996**, *126*, 227.
- [50] A. Hankin, F. E. Bedoya-Lora, J. C. Alexander, A. Regoutz, G. H. Kelsall, *J Mater. Chem. A* **2019**, *7*, 26162.
- [51] N. Hirayama, H. Nakata, H. Wakayama, S. Nishioka, T. Kanazawa, R. Kamata, Y. Ebato, K. Kato, H. Kumagai, A. Yamakata, K. Oka, K. Maeda, *J. Am. Chem. Soc.* **2019**, *141*, 17158.
- [52] J. Q. Li, L. Meng, J. Cheng, *J. Phys. Chem. C* **2022**, *126*, 578–587.
- [53] N. Vonrüti, U. Aschauer, *J. Mater. Chem. A* **2019**, *7*, 15741.
- [54] H. Kabbour, A. Sayede, G. Lefe, L. Cario, P. Roussel, *Chem. Commun.* **2020**, *56*, 1645.
- [55] X. Xiao, C. Liu, R. Hu, X. Zuo, J. Nan, L. Li, L. Wang, *J. Mater. Chem.* **2012**, *22*, 22840.
- [56] J. Li, H. Li, G. Zhan, L. Zhang, *Acc. Chem. Res.* **2017**, *50*, 112.
- [57] Cambridge Crystallographic Data Centre depository number 2073127.

Entry for the Table of Contents



Nanowires of the new oxychloride $\text{Zn}_4\text{Si}_2\text{O}_7\text{Cl}_2$ crystallize from molten salts as a polar three-dimensional tetrahedral framework. They exhibit strongly anisotropic charge carrier mobility, adjustable electrical properties, and photoelectrochemical properties for H_2 production from water.

Twitter handles:

@DavidPortehault

@INC_CNRS

@Nano_lcmcp

@ScienceSorbonne

Supporting Information
©Wiley-VCH 2021
69451 Weinheim, Germany

Molten Salts-Driven Discovery of a Polar Mixed-Anion 3D framework at the nanoscale: $\text{Zn}_4\text{Si}_2\text{O}_7\text{Cl}_2$, Charge Transport and Photoelectrocatalytic Water Splitting

Ram Kumar,^[a] Yang Song,^[a] Anissa Ghoridi,^[a] Philippe Boullay,^[b] Gwenaëlle Rouse,^[c] Christel Gervais,^[a] Cristina Coelho Diogo,^[d] Houria Kabbour,^[e] Capucine Sassoïe,^[a] Patricia Beaunier,^[f] Victor Castaing,^[g] Bruno Viana,^[g] Maria Luisa Ruiz González,^[h,i] José González Calbet,^[h,i] Christel Laberty-Robert,^[a] David Portehault*^[a]

-
- [a] Dr. R. Kumar, Y. Song, Prof. C. Gervais, Dr. C. Sassoïe, Prof. C. L. Robert, Dr. D. Portehault
Sorbonne Université, CNRS, Collège de France, Laboratoire de Chimie de la Matière Condensée de Paris (CMCP), 4 place Jussieu, F-75005, Paris, France
E-mail: david.portehault@sorbonne-universite.fr
- [b] Dr. P. Boullay
Normandie Université, ENSICAEN, UNICAEN, CNRS, CRISMAT, 14000 Caen, France
- [c] Dr. G. Rouse
PSL Research University, Sorbonne Université, Collège de France, Chimie du Solide et de l'Energie, UMR 8260, Collège de France, 11 place Marcelin Berthelot, 75007 Paris, France
- [d] Dr. C. Coelho Diogo
Sorbonne Université, CNRS, Institut des Matériaux de Paris-Centre, IMPC, F-75005, Paris, France
- [e] Dr. H. Kabbour
Univ. Lille, CNRS, ENSCL, Centrale Lille, Univ. Artois, UMR 8181-UCCS-Unité de Catalyse et de Chimie du Solide, F-59000 Lille, France
- [f] P. Beaunier
Sorbonne Université, CNRS, Laboratoire de Réactivité de Surface (LRS), 4 place Jussieu, F-75005, Paris, France
- [g] Dr. V. Castaing, Dr. B. Viana
PSL Research University, Chimie ParisTech, CNRS, Institut de Recherche de Chimie de Paris, 11 rue Pierre et Marie Curie, 75005 Paris, France
- [h] Dr. M. Luisa Ruiz Gonzalez, Prof. J. G. Calbet
Departamento de Química Inorgánica, Facultad de Químicas, Universidad Complutense, 28040-Madrid, Spain
- [i] Centro Nacional de Microscopía Electrónica, Universidad Complutense, 28040 Madrid, Spain

Table of Contents

Experimental Procedures		S-4-13
Figure S1	Scheme of the crystal structure of the silicon precursor Na_4Si_4	S-12
Figure S2	TGA traces of commercial ZnCl_2 and NaCl used for the synthesis	S-12
Figure S3	SEM images of $\text{Zn}_4\text{Si}_2\text{O}_7\text{Cl}_2$ nanowires	S-13
Figure S4	TEM image and corresponding selected area electron diffraction pattern (SAED) of $\text{Zn}_4\text{Si}_2\text{O}_7\text{Cl}_2$ nanowires	S-13
Figure S5	Energy-dispersive X-ray spectrum of nanowires	S-14
Figure S6	STEM-HAADF image and corresponding STEM-EDS maps of $\text{Zn}_4\text{Si}_2\text{O}_7\text{Cl}_2$ nanowires	S-14
Figure S7	TEM images of $\text{Zn}_4\text{Si}_2\text{O}_7\text{Cl}_2$ nanowires in solidified salt matrix before washing	S-15
Figure S8	TEM images of $\text{Zn}_4\text{Si}_2\text{O}_7\text{Cl}_2$ nanowires obtained at different reaction durations	S-15
Figure S9	Reconstructed reciprocal space sections	S-16
Table S1	Combined PEDT data sets to obtain a single data set used for the structure solution step	S-16
Figure S10	Electrostatic potential map obtained from <i>ab initio</i> structure solution using single nanowires PEDT datasets	S-17
Table S2	Crystallographic details of data reduction and dynamical refinement	S-18
Table S3	Structural parameters of the refinement based on PEDT	S-18
Table S4	List of selected interatomic distances and bond valence sums (BVS) of the refined model based on PEDT data	S-19
Table S5	Structural parameters for $\text{Zn}_4\text{Si}_2\text{O}_7\text{Cl}_2$ deduced from the Rietveld refinement of SXRD data	S-20
Figure S11	HRTEM images of $\text{Zn}_4\text{Si}_2\text{O}_7\text{Cl}_2$ nanowires.	S-21
Table S6	Known compounds in the polar orthorhombic $A2mm$ space group	S-21
Figure S12	^{35}Cl static solid-state NMR spectrum of $\text{Zn}_4\text{Si}_2\text{O}_7\text{Cl}_2$ nanowires	S-22
Figure S13	EELS spectrum of $\text{Zn}_4\text{Si}_2\text{O}_7\text{Cl}_2$ nanowires in the region of the Zn L_1 , L_2 and L_3 edges	S-22
Figure S14	High resolution X-ray photoelectron spectra of $\text{Zn}_4\text{Si}_2\text{O}_7\text{Cl}_2$ nanowires	S-23
Table S7	XPS peak assignment	S-24
Figure S15	Infrared spectrum of $\text{Zn}_4\text{Si}_2\text{O}_7\text{Cl}_2$ nanowires	S-25
Figure S16	PDF analysis of the powder X-ray scattering pattern	S-26
Figure S17	Si-2p XPS of $\text{Zn}_4\text{Si}_2\text{O}_7\text{Cl}_2$	S-27
Figure S18	Thermogravimetric analysis of $\text{Zn}_4\text{Si}_2\text{O}_7\text{Cl}_2$ nanowires	S-27

SUPPORTING INFORMATION

Figure S19	TEM images of $\text{Zn}_4\text{Si}_2\text{O}_7\text{Cl}_2$ nanowires exposed to different atmospheres	S-28
Figure S20	TEM images of $\text{Zn}_4\text{Si}_2\text{O}_7\text{Cl}_2$ nanowires exposed to different aqueous solutions	S-29
Figure S21	Luminescence properties of $\text{Zn}_4\text{Si}_2\text{O}_7\text{Cl}_2$ nanowires	S-30
Table S8	DFT full geometry optimization	S-30
Figure S22	DFT calculated band structure and effective masses of charge carriers	S-31
Table S9	Details of the calculations of the effective masses of charge carriers	S-31
Figure S23	Projected density of states	S-32
Figure S24	Powder XRD patterns of p-type $\text{Zn}_4\text{Si}_2\text{O}_7\text{Cl}_2$ synthesized in glass and n-type $\text{Zn}_4\text{Si}_2\text{O}_7\text{Cl}_2$ synthesized in a glassy carbon crucible	S-33
Figure S25	C 1s XPS of carbon-doped $\text{Zn}_4\text{Si}_2\text{O}_7\text{Cl}_2$	S-33
Figure S26	Linear sweep voltametry curves under chopped light at different pH values for $\text{Zn}_4\text{Si}_2\text{O}_7\text{Cl}_2$	S-34
Figure S27	EDS and XRD pattern of electrode after photoelectrochemical measurements	S-34
Figure S28	SEM, TEM and electron diffraction characterization of $\text{Zn}_4\text{Si}_2\text{O}_7\text{Cl}_2$ nanowires after chronopotentiometry	S-35
Figure S29	Photoelectrochemical cell setup and experiments for undoped $\text{Zn}_4\text{Si}_2\text{O}_7\text{Cl}_2$	S-35
Figure S30	Photoelectrochemical properties of $\text{Zn}_4\text{Si}_2\text{O}_7\text{Cl}_2$ nanowires synthesized in a glassy carbon crucible	S-36
Figure S31	<i>Post</i> electrochemistry morphological and structural characterization of $\text{Zn}_4\text{Si}_2\text{O}_7\text{Cl}_2$ nanowires synthesized in a glassy carbon crucible after chronopotentiometry	S-36
Additional references		S-37

SUPPORTING INFORMATION

Experimental Procedures

All the reagents and chemicals were used as obtained from commercial sources (Sigma Aldrich and Alfa Aesar). Si powder (99.99%, Sigma-Aldrich catalog no: 267414); dry NaH powder (90%, Sigma-Aldrich catalog no: 223441); anhydrous ZnCl₂ (99.95%, Alfa-Aesar catalog no: 87900); ZnCl₂ (99.999%, Sigma-Aldrich catalog no: 229997), methanol (99.9% Sigma-Aldrich catalog no: 34860), anhydrous Na₂SO₄ (≥99%, Sigma-Aldrich catalog no: 1.06649) and UHP grade argon (99.9999%, Air Liquide, ALPHAGAZ 2) as well as deionized Milli-Q water were used.

Synthesis of Na₄Si₄: All manipulations were performed inside an argon-filled glovebox. Na₄Si₄ was synthesized using a reported procedure with modifications.^[1] Si and NaH powders were mixed in 1:2.1 mole ratio and ball milled for 5 min at 20 Hz (Retsch MM400 ball mill airtight vials of 50 mL, one steel ball of 62.3 g and a diameter of 23 mm). The homogeneous mixture was transferred to a *h*-BN HPP crucible covered with a lid, subsequently inserted inside a quartz tube and heated in a vertical furnace at 420 °C for 96 h under argon. A brown-black pellet with a spongy white residue on top of it was obtained. The white residue corresponding to NaOH was carefully removed. The pellet was crushed to obtain a Na₄Si₄ powder. Powder X-ray diffraction, ²⁹Si and ²³Na MAS solid-state NMR confirmed the phase purity.^[2] The yield was 94% based on Si.

Synthesis of Zn₄Si₂O₇Cl₂ nanowires: The Zn₄Si₂O₇Cl₂ nanowires were synthesized in molten ZnCl₂-NaCl eutectic (ZnCl₂ = 68 mol. %, NaCl = 32 mol. %, m.p. = 260 °C). The ZnCl₂ powder consisted of ca. 87 mol. % ZnCl₂, 7 mol. % ZnCl₂·1.33H₂O and 4 mol. % of water according to TGA and XRD analysis. In a typical batch, 2.2 mmol NaSi and 60 mmol of ZnCl₂-NaCl eutectic mixture was ball milled together for 2 min at 20 Hz (Retsch MM400 ball mill airtight vials of 50 mL, one steel ball of 62.3 g and a diameter of 23 mm). The mixture was subsequently transferred to a glass tube (or a glassy carbon crucible in case of carbon-doping) and heated at 420 °C under argon for 4 h. The effect of reaction time was studied by performing the reaction for different duration (1h to 100h). Zn₄Si₂O₇Cl₂ nanowires were always obtained although an increased reaction time resulted in increased aspect ratio. The nanowires quenched in the salt matrix were washed with a copious amount of deionized water and dried under vacuum. The yield of nanowires was 47% based on Si. 21 batches of Zn₄Si₂O₇Cl₂ nanowires were synthesized with varying reaction time, several batches of Na₄Si₄ and two different commercial sources of ZnCl₂ (99.95% Alfa Aesar catalog no. 87900 and 99.999% Sigma-Aldrich catalog no. 229997) and with two different experimenters to ensure reproducibility.

Powder X-ray diffraction, structure refinement: Synchrotron X-ray diffraction (SXR) was performed at the 11-BM beamline (Advanced Photon Source, Argonne National Laboratory). The powder was placed in a 0.7 mm diameter sealed glass capillary. Patterns were collected in transmission mode with

SUPPORTING INFORMATION

$\lambda = 0.412831 \text{ \AA}$. All patterns were refined using the Rietveld method as implemented in the FullProf program.^[3] X-ray powder diffraction (XRD) patterns were performed on pristine samples using a BRUKER D8 Advance diffractometer equipped with Cu K α radiation source ($\lambda \text{ K}\alpha_1 = 1.54056 \text{ \AA}$, $\lambda \text{ K}\alpha_2 = 1.54439 \text{ \AA}$).

Pair distribution function analysis (PDF):

Data collection and sample preparation. X-ray total scattering data were measured with a Bruker D8 ADVANCE diffractometer equipped with a focusing Göbel mirror and a LYNXEYE detector, with Mo K α radiation (mean $\lambda(\text{K}\alpha_1\alpha_2) = 0.71073 \text{ \AA}$) at room temperature. Few tens of milligrams of powder are placed in a thin-walled (0.01 mm) borosilicate glass capillary of 0.5 mm diameter. Measurements were performed from $Q_{\min} = 0.12 \text{ \AA}^{-1}$ to $Q_{\max} = 17.0 \text{ \AA}^{-1}$ ($Q = 4\pi \sin \theta/\lambda$) with sample rotation around its axis and evolving counting parameters in function of Q-range to optimize the counting rate at high Q. The final XRD diagram was thus obtained from the combination of 7 patterns, converted in counts per second, with the following parameters $2\theta_i(^{\circ})$ - $2\theta_f(^{\circ})$ -step size($^{\circ}$)-step time(s): 0.8-31-0.02-2, 29-61-0.04-6, 59-91-0.06-15, 89 121 0.1 40 (twice) and 119-150-0.1 100 (twice) for a total measuring time of 34 hours. Additional scattering measurements from empty capillary were performed in the same conditions for background subtraction. Raw data were treated using the PDFgetX3 program.^[4] Standard corrections were applied to the total scattering data. After a normalization step, they were reduced into the structure function. The experimental PDF $G(r)$ is finally obtained by a Fourier Transform (FT).

PDF calculations from structural models. The simulated $\text{Zn}_4\text{SiO}_7\text{Cl}_2$ PDF profile was calculated using the PDFgui software with periodic boundary conditions.^[5] The structural model from PEDT refinement was used. Given the large size of the cell and the high number of atoms, the atomic positions were fixed, and only isotropic atomic displacements, scale and width parameters were allowed to vary during the refinement.

Additional PDF profiles were also calculated in order to detect possible amorphous impurities: Cif files were directly used from database with stepcut parameter of 2.5 \AA meaning that the calculated PDF is truncated and fixed to zero above this value to mimic the absence of correlation peak at higher distance r in an amorphous phase.

Precession-assisted electron diffraction tomography and structure analysis from PEDT data.

Precession-assisted electron diffraction tomography (PEDT), was performed with a JEOL 2010 transmission electron microscope (operating at 200 kV with a LaB $_6$ cathode) equipped with a Nanomegas DigiStar precession module and an upper-mounted Gatan ORIUS 200D CCD camera. PEDT aims a three-dimensional reconstruction of the reciprocal space by tilting sequentially the sample and recording at each step a precession electron diffraction patterns. PEDT data sets of non-oriented patterns were recorded on several nanowires. For data collections the precession angle was set to 1.2° with a goniometer tilt step 1° . PEDT data sets were analyzed and diffracted intensities integrated using the

SUPPORTING INFORMATION

program PETS 2.0^[6]. The structure solution step was performed in JANA2006^[7] using *ab initio* phasing by charge-flipping^[8] from the combination of two PEDT data sets (details in **Table S1**) with an overall completeness of 99.4 % for a resolution shell $\sin(\theta_{\max})/\lambda = 0.65$. The resulting electrostatic potential map (**Figure S9**) allows obtaining unambiguously a structural model containing 20 atomic positions. The subsequent structure refinement taking into account both dynamical diffraction effects and the precession motion was conducted in JANA2006. Details about this so-called “dynamical refinement” procedure applied to PEDT data are given elsewhere.^[9] In this step the structural model is refined simultaneously against the two PEDT data sets (**Table S1**) leading to a global R_{obs} value of about 16% (**Table S2**) and the structural parameters given in **Table S3**. Examining the interatomic distances and bond valence sums listed in **Table S4**, the refined structure obtained without any distance restrains is quite coherent.

STEM-HAADF and STEM-EDS mapping: Scanning TEM high-angle annular dark-field (STEM-HAADF) and scanning TEM-Energy Dispersive X-ray Spectroscopy (STEM-EDS) microanalysis for chemical mapping were carried out on a JEOL JEM 2100Plus TEM microscope, operating at 200 kV, interfaced to Oxford Instrument Aztec EDS system with an X-Max T large area (80 mm²) SDD detector.

SEM and EDS analysis was performed on a Hitachi SU-70 equipped with Oxford instruments EDS accessories.

HRTEM and EELS: High Resolution Transmission Electron Microscopy (HRTEM) images were obtained in a JEOL-JEM GRAND ARM 300 cF microscope equipped with a Cs Corrector (ETA-JEOL). The accelerating voltage was set to 80 kV in order to minimize the sample damage. The HRTEM images were acquired using a one view CMOS camera (4096 x 4096 pixels, Gatan OneView Camera). EELS spectra were acquired in a probe spherical aberration corrected microscope JEOL JSM-ARM200F at 80 kV equipped with a GIF-QuantumERTM spectrometer (with a collection semiangle of 18 mrad and a convergence semiangle of 20.3 mrad). The spectra were obtained using the line scan mode, in different areas in order to minimize the beam damage and gain reliability, with a spatial resolution of ~0.05 nm over a total acquisition time of one minute with an energy dispersion of 0.4 eV per channel. Two energy windows were simultaneously used (DUAL EELS) to get the Si-L, O-K and Zn-L edges. EELS Principal component analysis was always performed on EELS data set to de-noise the spectra by using the MSA plug-ins for Gatan DMS analysis toolbox.^[10]

X-ray photoelectron spectroscopy (XPS): The powders were deposited on a clean indium substrate to form a uniform layer fully covering the conducting substrate. Subsequently, the sample was transferred into an ultrahigh vacuum (UHV) chamber with a base pressure 2×10^{-10} Torr. The XPS spectra were recorded on a Scienta Omicron photoelectron spectrometer using monochromatic Al $K\alpha$ (1486.6 eV) as the X-ray source having a 300 W electron beam power at 2×10^{-10} Torr vacuum pressure. Binding energies were calibrated against the C 1s (C-C) binding energy at 284.8 eV. High-resolution XP spectra were collected at a pass energy of 20 eV and the general spectra were collected with steps of 100 eV.

SUPPORTING INFORMATION

The atomic ratio calculations were performed after normalization using Scofield factors. Spectra processing was carried out using the Casa XPS software package with Shirley background correction.

NMR: ^{29}Si MAS NMR experiments were performed on a 700 MHz AVANCE III Bruker spectrometer operating at 139.1 MHz, using a 3.2 mm Bruker probe spinning at 20 kHz. A single-pulse excitation with a flip angle of 90° and a recycle delay of 500 s were used. ^{35}Cl NMR experiments were performed at 68.6 MHz using a 5 mm static probe. A WURST-QCPMG^[11] pulse sequence was used to deal with the very broad lineshapes produced by significant quadrupolar interaction, using recycle delays of 2s, 56 echos with a duration of 50 s and 6400 scans. ^{29}Si and ^{35}Cl spectra were referenced to tetramethylsilane (TMS) and NaCl respectively. Spectra were fitted with the DMFIT program.^[12]

Thermogravimetric analysis was carried out using a NETZSCH apparatus under air or nitrogen at a heating rate of $5\text{ }^\circ\text{C min}^{-1}$.

The **infrared spectrum** was recorded using a PerkinElmer-100 ATR in ATR mode.

Photoluminescence (PL) and lifetime measurements were performed using an optical parametric oscillator (Ekspla NT OPO Laser) pulsed laser as the excitation source. The excitation wavelength was set at 230 nm. The acquisition of the emission spectra was held by a CCD camera (Princeton Instruments, PI-MAX4) coupled to a monochromator (Princeton Instruments, Acton SpectraPro 2300 with a 300 grooves per mm grating). The low temperature (10 K) was set using a closed-cycle cryostat (Sumitomo Cryogenics) coupled with a temperature controller (Lakeshore 340). To record the lifetime measurements the same monochromator (centered at 450 nm) was used coupled to a Hamamatsu photomultiplier tube.

Diffuse reflectance UV-Visible spectra were recorded using Agilent Cary 5000 UV-vis spectrometer with integrating sphere accessory. The powder sample was placed inside the sample holder with an optical grade quartz window to form a thick layer and the spectra were recorded in diffuse reflectance mode.

Nitrogen adsorption-desorption measurements and corresponding BET calculations were obtained at 77 K using a BELSORB-max apparatus, with the powder previously evacuated at $120\text{ }^\circ\text{C}$ for 18 h.

Photoelectrochemical measurements. The electrodes for the photoelectrochemical measurements were prepared on fluorine-doped tin oxide (FTO) substrates. The FTO substrate was obtained from Asahi Glass, Japan. The thickness of FTO coating on glass was 700 nm with a conductivity of $8\ \Omega/\text{sq}$. The FTO substrates were cleaned by ultrasonication in deionized water, absolute ethanol and dried prior to the drop-casting. The $\text{Zn}_4\text{Si}_2\text{O}_7\text{Cl}_2$ nanowires (20 mg) was dispersed by sonication in ethanol (2.3 mL), ethylene glycol (190 μL) and Triton-X (10-15 μL), (~2.5 mL dispersion). The obtained homogeneous dispersion ($\approx 0.5\text{ mL}$) was drop casted on an FTO substrate to make a uniform film with a catalyst loading of $4\pm 1\text{ mg}$ over a $\sim 1\text{ cm} \times 1\text{ cm}$ area. The solvents were evaporated by heating at $120\text{ }^\circ\text{C}$ for approx. 5 h in a hot air oven. The uniform dry film was subsequently annealed at $300\text{ }^\circ\text{C}$ for 5 min in air to remove the organics. The obtained electrodes were attached with a conducting wire using adhesive copper tape

SUPPORTING INFORMATION

and covered with 3M insulating tape to select a 0.785 cm² active area. A hole with 1 cm circular diameter was punched in a 3M electrolytic insulating tape to select an active area of ca. 0.79 cm². Photoelectrochemical experiments were performed using a Solartron ModuLab electrochemical workstation

The photoelectrochemical measurements were performed in an optical grade quartz photoreactor cell with quartz windows transparent to UV-visible light. An Ag/AgCl/Sat. KCl electrode was used as reference. The photoelectrochemical cell encompassed two compartments, one for the working electrode and another for the Pt counter electrode. Both compartments were separated by a frit (**Figure S29**). For hydrogen quantification experiments a photoelectrode of (1 cm X 2 cm) was used. The photoelectrochemical cell was sealed with rubber septa (Sigma-Aldrich) and an additional parafilm layer wrapping. The 0.1 mol L⁻¹ Na₂SO₄ electrolyte solution was purged by argon bubbling for 2 h with a flow rate of about 75 mL min⁻¹ through a needle, with an extra needle placed on top of the rubber septum to vent out the overpressure. Ar purge was stopped during the experiment. The electrolyte solution was stirred during the measurements. The measurements were performed at 25 °C.

The evolved H₂ was analysed using a gas chromatograph (GC, Multi-Gas Analyser, SRI Instruments). The samples were withdrawn at a regular interval of 30 minutes by using a Hamilton gastight syringe with a Luer lock. For each aliquot, the syringe was inserted inside the photoelectrochemical cell through the rubber septum. 50 µL gas was withdrawn from the headspace and then injected inside the GC column for H₂ analysis. Argon was the carrier gas, H₂ was separated with a HaySepD precolumn followed by a molecular sieve column, and detected with a thermal conductivity detector (TCD) operating at 220 °C. The GC was calibrated at five points with gas samples of known concentrations of H₂ in CO₂. Linear fitting through these five points was used to recover a calibration curve further used for H₂ quantification. The measured applied potential was converted to the reversible hydrogen electrode (RHE) potential using the equation $E_{RHE} = [E^0_{Ag/AgCl} + E_{Ag/AgCl} + 0.059 \times pH]$. The pH of the 0.1 M Na₂SO₄ electrolyte solution was measured to be 7 with a pH-meter (ThermoFisher Scientific) freshly calibrated at three pH points 4, 7 and 10. Faradaic efficiency was calculated using the equation $Faradaic\ efficiency = (moles\ of\ H_2\ produced) \times 2 / (moles\ of\ electrons)$. The uncertainty of Faradaic efficiency was evaluated at 10 % for each measurement due to cumulated uncertainties of volume measurements. The photoelectrochemical measurements were repeated 3 times to ensure reproducibility. We then evaluate the uncertainty on the mean value at ±14%, thus yielding a Faradaic efficiency of (85±14)%. The incident photon to current conversion efficiency (IPCE) was measured at different monochromatic wavelengths in the UV-visible region. The monochromatic light at different wavelengths in the UV-visible region was obtained by using optical bandpass filters (Newport) at different wavelengths in the visible and UV region. The FWHMs of the bandpass filters (Newport) were 10 nm–12 nm. The same 280 W Xe arc lamp was used as light source (100 mW cm⁻² illuminated intensity) and the optical bandpass filters were placed using a stand on the light beam path to achieve

SUPPORTING INFORMATION

monochromatic light irradiation of the photoelectrochemical cell. The incident power at each wavelength was measured using an optical detector and power-meter from Newport instruments (Newport 1919-R optical power-meter connected to a 200-1100 nm Newport optical power detector (918D-UV-OD3R)). The photoresponse at each wavelength and the corresponding power of the incident light were recorded. The IPCE was calculated employing the formula $IPCE \% = [I (\mu A/cm^2) \times 1240 \times 100] / [P (\mu W/cm^2) \times \lambda (nm)]$. The same configuration was used to record linear sweep voltammetry curves under chopped light (Figure S26).

The electrochemical impedance data were recorded with a Modulab Solartron potentiostat at a frequency of 100 kHz. The electrode was prepared as described above.

DFT calculations were carried out in order to investigate the structure and electronic structure of $Zn_4Si_2O_7Cl_2$. The projector augmented wave (PAW)^[15,16] method encoded in the Vienna ab initio simulation package (VASP)^[17] and the generalized gradient approximation (GGA) of Perdew, Burke and Ernzerhof (PBE) for the exchange-correlation functionals^[18] were employed. The lattice constants and the atomic coordinates were fully optimized using a plane wave energy cutoff of 550 eV and 20 *k* points in the irreducible Brillouin zone. The structure relaxation was performed until the force on each atom became smaller than 0.03 eV Å⁻¹. It led to slightly increased unit cell parameters of *a*=5.2648 Å (+1.6%), *b*=18.0190 Å (+1.2 %) and *c*=20.9947 Å (+ 1%) in space group *A2mm*, in good agreement with the experimental ones of *a* = 5.184172(12) Å, *b* = 17.7897(2) Å and *c* = 20.7771(3) Å, i.e. within a reasonable error expected for the GGA method. The relaxed structure was used for calculations of the electronic structure. For the later, the number of *k* points (see table below) in the irreducible Brillouin Zone was increased to 96 and the threshold of self-consistent-field energy convergence was set to 10⁻⁶ eV. The dipole moment was calculated according to a procedure described in the literature.^[19]

List of the high symmetry *k*-points (and their positions) used for the *k*-path in the Brillouin zone for the band structure calculation.

A	0.4332817427	0.4332817427	0.5000000000
C ₀	-0.4332817427	0.5667182573	0.0000000000
E ₀	-0.4332817427	0.5667182573	0.5000000000
Γ	0.0000000000	0.0000000000	0.0000000000
R	0.0000000000	0.5000000000	0.5000000000
S	0.0000000000	0.5000000000	0.0000000000
Σ ₀	0.4332817427	0.4332817427	0.0000000000
T	-0.5000000000	0.5000000000	0.5000000000
Y	-0.5000000000	0.5000000000	0.0000000000
Z	0.0000000000	0.0000000000	0.5000000000

NMR: The theoretical ²⁹Si and ³⁵Cl NMR parameters were investigated within the DFT framework, using periodic boundary conditions and the generalized gradient approximation (GGA) to the exchange-

SUPPORTING INFORMATION

correlation functional as proposed by Perdew, Burke and Ernzerhof (PBE).^[18] The NMR chemical shift describes the difference between the applied external magnetic field and the magnetic field at the nucleus positions. It can be obtained on the structural model by calculating the shielding of the nuclei relative to the electronic current induced by the external magnetic field. This current was calculated by using the GIPAW approach, which allows reconstructing the all-electron magnetic response from the pseudo-wave-functions.^[20,21] The calculations were performed using the PWscf and GIPAW codes of the Quantum ESPRESSO package.^[22] Norm-conserving pseudo-potentials were used and the wave functions kinetic energy cutoff was increased to 80 Ry.

The isotropic chemical shift δ_{iso} is defined as $\delta_{\text{iso}} = -(\sigma - \sigma^{\text{ref}})$, where σ is the isotropic shielding (one-third of the trace of the NMR shielding tensor) and σ^{ref} is the isotropic shielding of the same nucleus in a reference system. In our calculations, absolute shielding tensors are obtained. To fix the scales, σ^{ref} was chosen by comparing averaged experimental and calculated δ_{iso} values of sodium silicates for ^{29}Si as well as organic and inorganic chlorides for ^{35}Cl .

SUPPORTING INFORMATION

Structure resolution. PEDT measurements on different nanowires have revealed signs of diffuse scattering (**Figure S8**) indicating some structural disorder. By examining the reconstructed reciprocal space of several crystals, we retained a A-centered orthorhombic lattice with unit cell parameters $a \approx 5.2 \text{ \AA}$, $b \approx 17.5 \text{ \AA}$ and $c \approx 20.7 \text{ \AA}$. For *ab initio* structure solution (charge flipping method^[8]), the measurements performed on two nanowires were combined to obtain a data set with high completeness (**Table S1**). Symmetry analysis^[23] of the solution indicated that the *A2mm* group appeared more probable than the centro-symmetric *Ammm* group (symmetry agreement factor around 20 for mirror *m* versus 10 for axis 2). Both possibilities have been considered, but only the *A2mm* space group leads to a plausible structure with 21 independent atoms clearly revealed from the electrostatic potential map (**Figure S9**). Taking dynamical diffraction effects into account,^[9] the structural model was refined (**Tables S2** and **S3**) considering the stoichiometry $\text{Zn}_4\text{Si}_2\text{O}_7\text{Cl}_2$. Interatomic distances and bond valence strength calculations (**Table S4**) strongly support the structure proposed for this new oxychloride. One can identify ZnO_3Cl tetrahedra bridged by Cl atoms (**Figure 1D-H**) with Zn-Cl-Zn angles ranging between 105.8° to 114.6° . $(\text{ZnO}_3)_2\text{Cl}$ dimers are bridged by corner-sharing SiO_4 tetrahedra, also forming $(\text{SiO}_3)_2\text{O}$ dimers. The polar axis is the *a* axis along which all tetrahedra are oriented (**Figure 1F**), also corresponding to the axis of channels delimited alternatively by 7 tetrahedra ($4\text{Zn}+3\text{Si}$) and 6 tetrahedra ($4\text{Zn}+2\text{Si}$). In the latter case, one chlorine atom points towards the center of the channels. To check the consistency between the structure obtained from a few nanowires and the whole powder, a Rietveld analysis was conducted using a synchrotron powder XRD (SXR) pattern (**Figure 2A**, $R_{\text{Bragg}} = 8.37\%$, $\chi^2 = 1.72$). The refined lattice parameters are $a = 5.184172(12) \text{ \AA}$, $b = 17.7897(2) \text{ \AA}$ and $c = 20.7771(3) \text{ \AA}$, and all atomic positions were refined except the *x* position of O3 which serves as floating origin for the *x* axis for the *A2mm* space group. Atomic displacement parameters (ADPs) were considered as isotropic and constrained at the same values for identical chemical species. The resulting structure is in agreement with PEDT data (**Table S5**). However, the atomic positions deduced from Rietveld refinement lead to slightly more distorted ZnO_3Cl and SiO_4 tetrahedra than from PEDT, which is attributed to structural disorder and fluctuations in atomic positions from one crystallite to another. Anisotropic size broadening of the peaks was taken into account using spherical harmonics, and the reconstructed crystallites are needle-like shaped grown along the $[100]$ direction (**Figure 2A**). The diameter of the needle-like crystallites is found at *ca.* 16 nm, with length about ten-times larger, resulting in sharp (*h*00) reflections. This is in full agreement with high resolution transmission electron microscopy (HRTEM) (**Figures 1** and **S10**) that shows nanowires growing along the *a* axis of the channels.

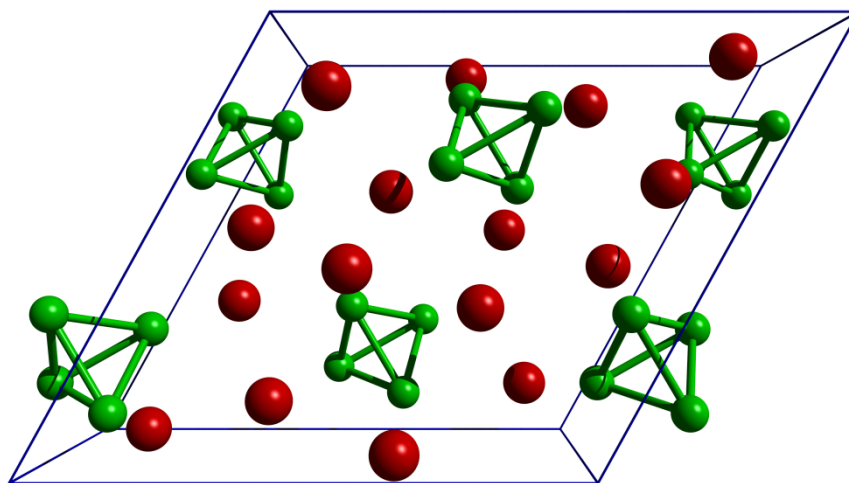


Figure S1. Schematized Na₄Si₄ structure encompassing tetrahedral [Si₄]⁴⁻ units (green) and Na⁺ cations (red spheres).

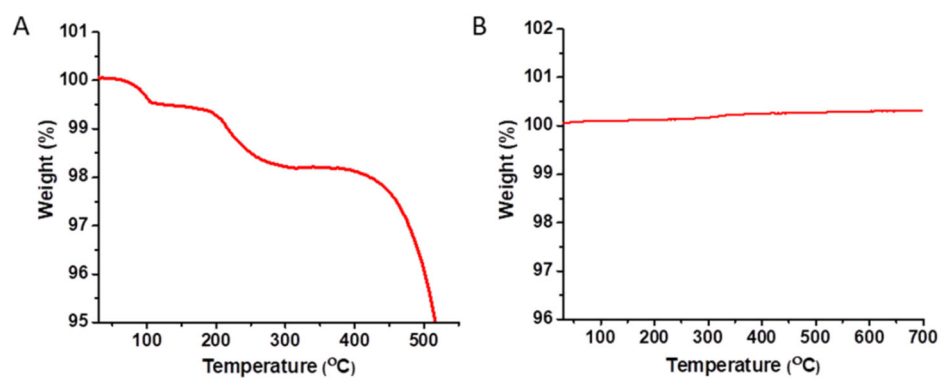


Figure S2. TGA traces under argon of commercial (A) ZnCl₂ and (B) NaCl used for synthesis. For ZnCl₂, the mass loss at ca. 100 °C is attributed to water evolution, the second one is attributed to dehydration of ZnCl₂·1.33H₂O, identified by an XRD pattern of the initial powder.

SUPPORTING INFORMATION

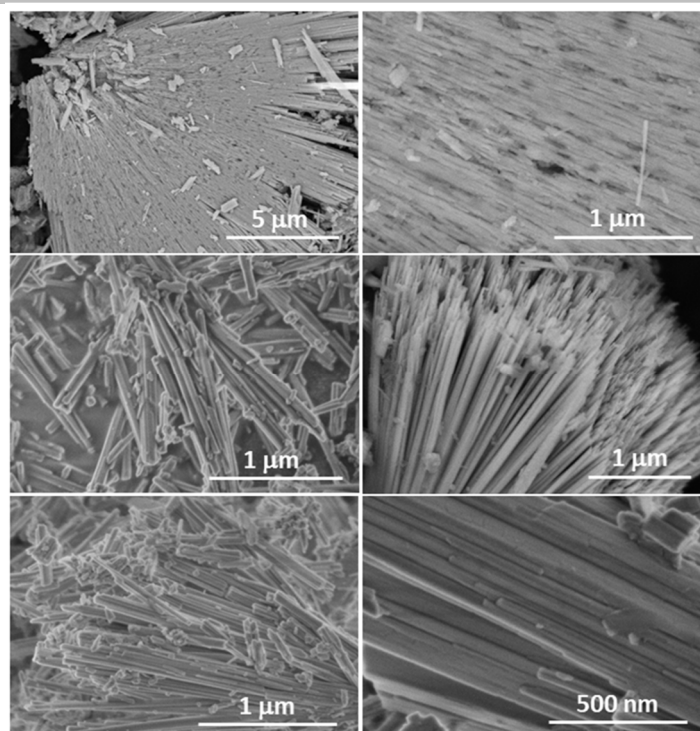


Figure S3. SEM images of nanowires obtained from the reaction of Na_4Si_4 in molten $\text{ZnCl}_2\text{-NaCl}$ at $420\text{ }^\circ\text{C}$ under argon.

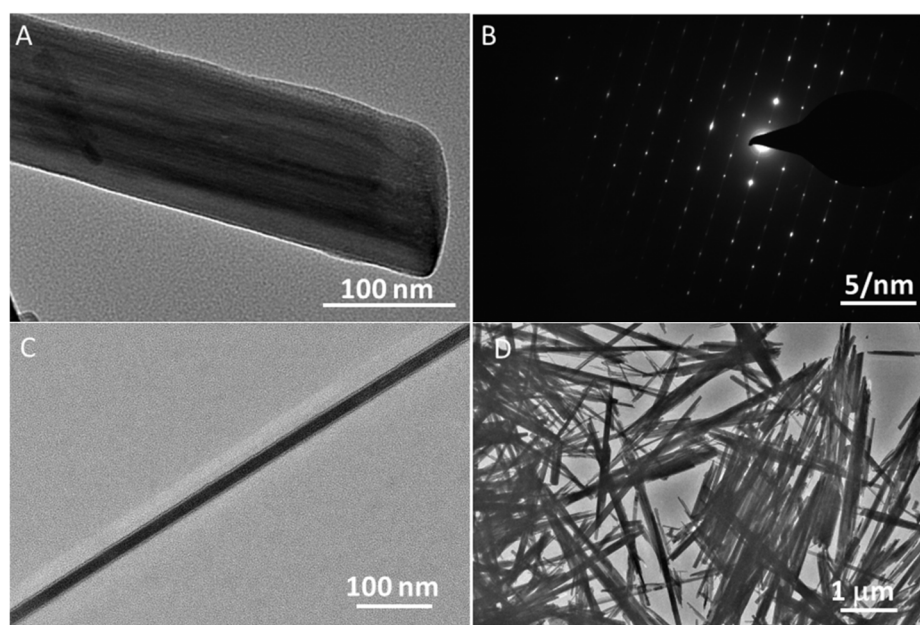


Figure S4. (A, B) TEM image and corresponding selected area electron diffraction pattern (SAED) of nanowires obtained from the reaction of Na_4Si_4 in molten $\text{ZnCl}_2\text{-NaCl}$ at $420\text{ }^\circ\text{C}$ under argon. (C, D) Low-magnification TEM images of the nanowires showing a high aspect ratio.

SUPPORTING INFORMATION

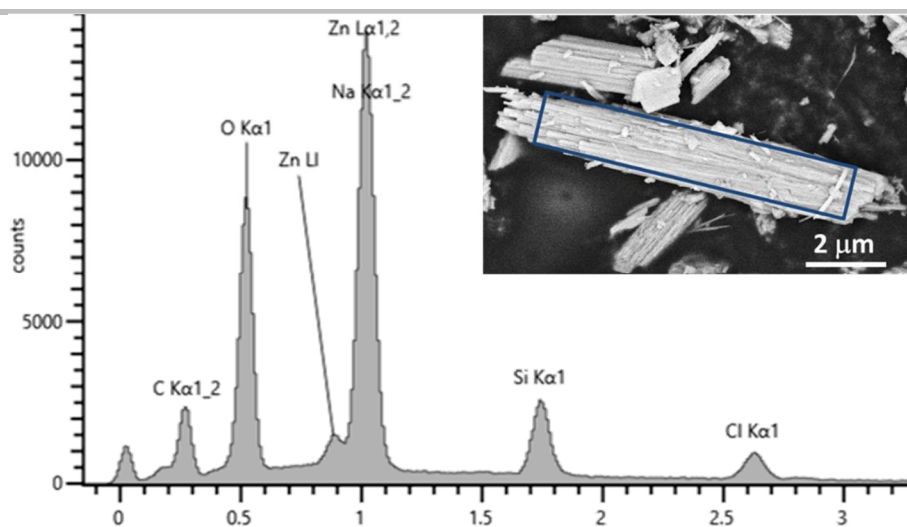


Figure S5. Energy-dispersive X-ray spectrum (EDS) of a bundle of nanowires. The average composition across the highlighted area is $(\text{Na})_{0.17}\text{Zn}_4\text{Si}_{2.2}\text{O}_{6.4}\text{Cl}_{1.9}$, giving an approximate composition Zn:Si:Cl = 4:2:2. Trace amounts of Na may originate from remaining salt traces at the surface of the nanowires or doping. Note also the difficult evaluation of the Na K peak that is overlapping with the Zn L peak.

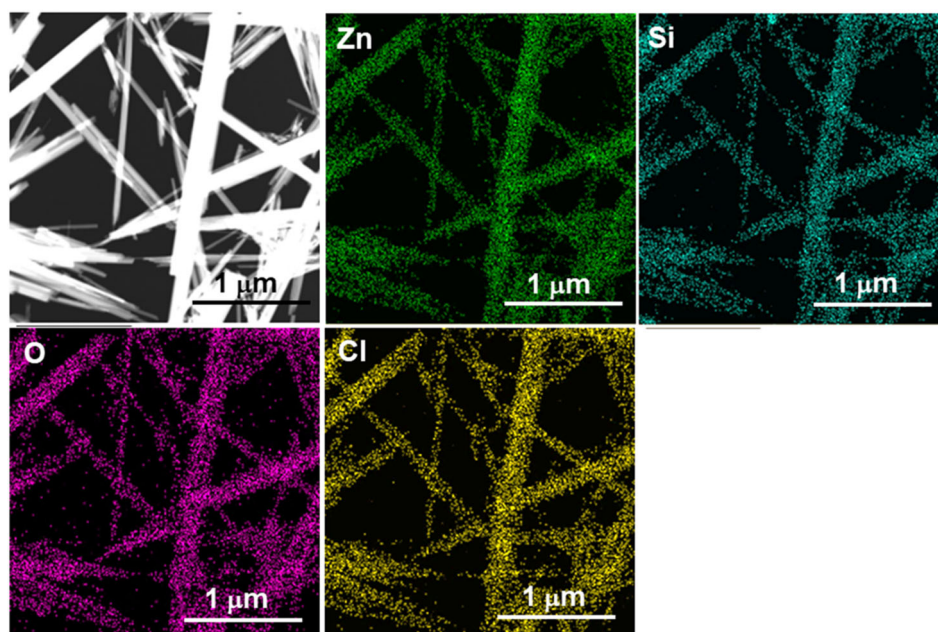


Figure S6. STEM-HAADF (top left) image and corresponding STEM-EDS maps of nanowires obtained from the reaction of Na_4Si_4 in molten ZnCl_2 - NaCl at 420 °C under argon.

SUPPORTING INFORMATION

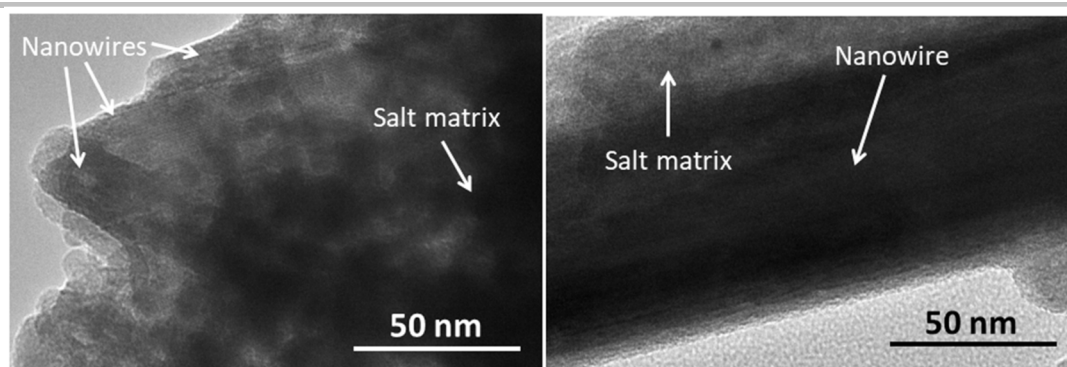


Figure S7. TEM images of nanowires obtained from the reaction of Na_4Si_4 in molten $\text{ZnCl}_2\text{-NaCl}$ at 420°C under argon, still embedded in the salt matrix before washing.

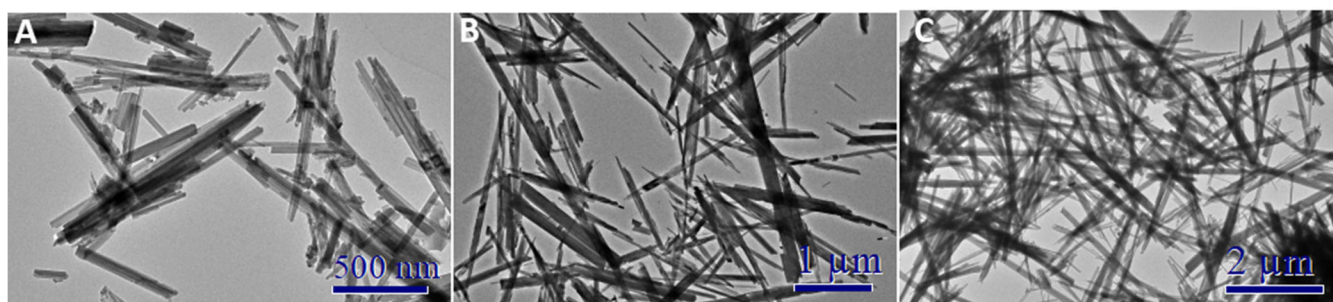


Figure S8. TEM images of $\text{Zn}_4\text{Si}_2\text{O}_7\text{Cl}_2$ nanowires obtained at different reaction durations and thermal annealing. (A) 4 h reaction, (B) 100 h reaction, (C) 96 h reaction followed by annealing at 500°C for 7 days under argon.

SUPPORTING INFORMATION

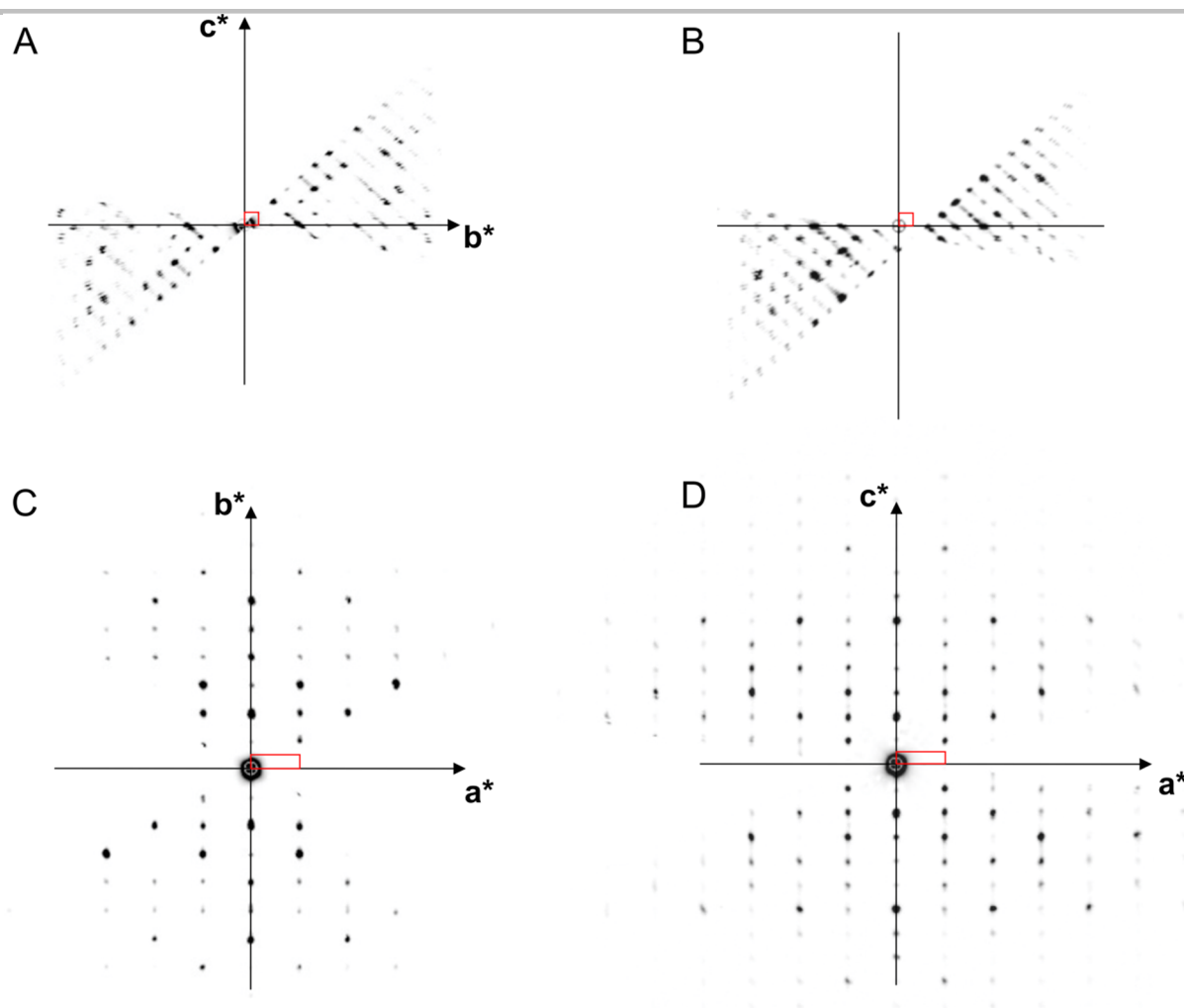


Figure S9. Reconstructed reciprocal space sections: (A) $0kl$ section and (B) $1kl$ section in which diffuse streaks are clearly visible. (C) $hk0$ section. (D) $h0l$ section. Examination of systematic absence in these sections allows us to propose an orthorhombic A-centered lattice. The retained unit cell is outlined in red.

Table S1. To increase completeness and redundancy 2 PEDT data sets were combined to a single data set used for the structure solution step. During the dynamical refinement procedure the structural model is refined simultaneously against the 2 data sets resulting in reliability factors for each data set and a global one (All).

Data set	No. of frames	No. of obs./all reflections	Compl. (%)	$\sin(\theta_{\max})/\lambda$	$R(\text{obs})$	$wR(\text{all})$	Average thickness (nm)
1	48	2711/4687	66.1	0.65	0.154	0.166	23.8 (4)
2	72	3852/6550	69.4	0.65	0.163	0.180	19.9 (3)
All	120	6563/11237	99.4	0.65	0.159	0.174	

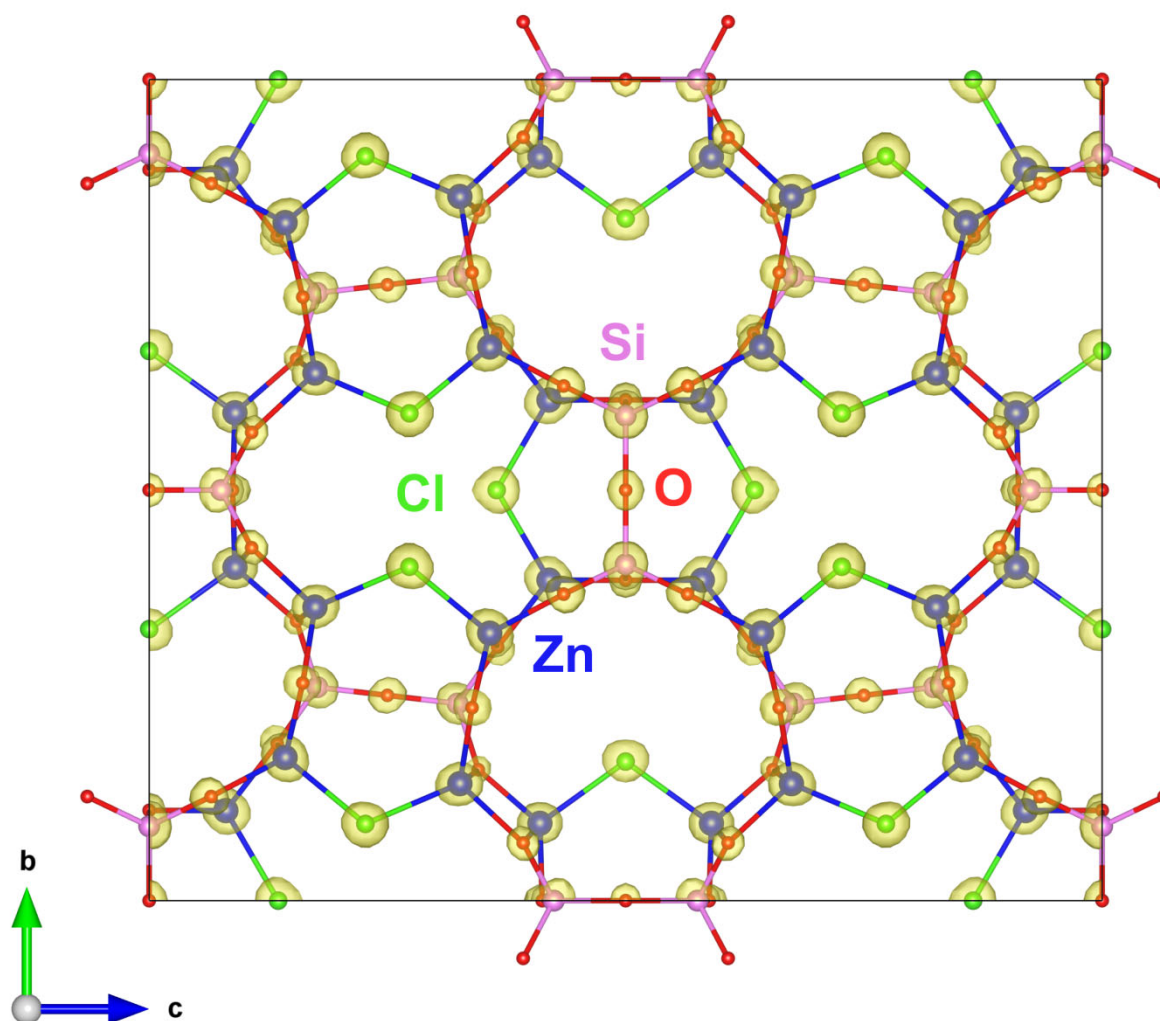


Figure S10. Electrostatic potential map obtained from *ab initio* structure solution using single nanowires PEDT datasets. In this projection along *a*, isosurface levels are plotted together with the deduced atomic positions (Cl = green, O = red, Zn = blue, Si = pink). Zn-Cl, Zn-O and Si-O bonds are included for clarity.

SUPPORTING INFORMATION

Table S2. Crystallographic details of data reduction and dynamical refinement. Software used for data reduction and structure refinement: PETS 2.0 [6] and Jana2006.[7]

Chemical formula	Zn ₄ Si ₂ O ₇ Cl ₂
Temperature (K)	293
Crystal system, space group	Orthorhombic, <i>A2mm</i>
<i>a</i> , <i>b</i> , <i>c</i> (Å) (taken from SXRD)	5.1842, 17.790, 20.777
<i>V</i> (Å ³)	1915.9
Electron wavelength λ (Å)	0.0251
Number of frames	120
Tilt step (°)	1.0
Precession angle (°)	1.2
$\sin(\theta_{\max})/\lambda$ (Å ⁻¹)	0.65
Completeness (%)	99.4
No. of measured, observed [$>3\sigma(I)$] reflections	11237, 6563
No. of refined parameters, restraints	167, 0
g_{\max} (Å ⁻¹), $S_{g,\max}$ (Å ⁻¹), R_{sg} , integration steps	1.6, 0.01, 0.4, 96
$R(\text{obs})$, $R(\text{all})$, $wR(\text{all})$, GoF(all)	0.159, 0.212, 0.174, 4.8

Table S3. Structural parameters of the refinement based on PEDT. Site occupancy are all equal to 1.

Atom label	<i>x</i>	<i>y</i>	<i>z</i>	U_{iso} (Å ²)
Zn1	0.806(2)	0.10945(15)	0.08005(12)	0.0054(6)
Zn2	0.307(2)	0.17333(16)	0.14330(13)	0.0103(6)
Zn3	0.321(2)	0.35799(16)	0.17391(13)	0.0093(6)
Zn4	0.822(2)	0.40572(17)	0.08841(15)	0.0147(7)
Cl1	0.718(2)	0	0.1360(3)	0.0179(16)
Cl2	0.206(2)	0.4047(3)	0.2735(2)	0.0117(10)
Cl3	0.771(3)	0.3290(4)	0	0.035(2)
Si1	0.304(3)	0.0909(3)	0	0.0035(7)*
Si2	0.319(3)	0.5	0.0727(3)	0.0035
Si3	0.806(2)	0.2596(2)	0.1758(2)	0.0035
O1	0.123(3)	0.2633(4)	0.1653(4)	0.0009(6)**
O2	0.618(3)	0.1135(6)	0	0.0009
O3	0.25***	0	0	0.0009
O4	0.173(3)	0.1251(4)	0.0649(3)	0.0009
O5	0.729(3)	0.25	0.25;	0.0009
O6	0.171(2)	0.4325(4)	0.1054(3)	0.0009
O7	0.660(3)	0.1925(4)	0.1325(4)	0.0009
O8	0.617(3)	0.5	0.0871(5)	0.0009
O9	0.186(3)	0.5	0	0.0009
O10	0.687(2)	0.3422(4)	0.1596(3)	0.0009

* All Si U_{iso} were constrained to be identical.** All O U_{iso} were constrained to be identical.

*** fixed parameter

SUPPORTING INFORMATION

Table S4. List of selected interatomic distances and bond valence sums (BVS) of the refined model based on PEDT data.

Atom 1	Atom 2	<i>d</i> (Å)	Multiplicity	BVS
Zn1	Cl1	2.314(5)	1	1.93(3)
	O2	1.928(10)	1	
	O4	1.947(18)	1	
	O7	1.985(10)	1	
Zn2	Cl2	2.277(6)	1	2.10(3)
	O1	1.920(11)	1	
	O4	1.969(9)	1	
Zn3	O7	1.877(17)	1	1.76(3)
	Cl2	2.309(7)	1	
	O1	1.981(12)	1	
	O6	2.093(10)	1	
Zn4	O10	1.940(17)	1	1.92(3)
	Cl3	2.304(6)	1	
	O6	1.908(17)	1	
	O8	1.983(10)	1	
Si1	O10	1.989(9)	1	3.81(6)
	O2	1.68(2)	1	
	O3	1.642(7)	1	
Si2	O4	1.626(11)	2	4.29(8)
	O6	1.579(11)	2	
Si3	O8	1.576(19)	1	3.84(6)
	O9	1.660(10)	1	
	O1	1.659(18)	1	
	O5	1.602(7)	1	
	O7	1.673(11)	1	
	O10	1.629(10)	1	

SUPPORTING INFORMATION

Table S5. Structural Parameters for $\text{Zn}_4\text{Si}_2\text{O}_7\text{Cl}_2$ deduced from the Rietveld refinement of the SXRD pattern, starting from the model obtained from PEDT. Isotropic temperature factors (B_{iso}) were constrained to be equal for the same chemical species. *The x coordinate of O3 was not refined because it serves as floating for the $A2mm$ space group. The atomic positions deduced from Rietveld refinement lead to slightly more distorted ZnO_3Cl and SiO_4 tetrahedra than from PEDT, which is attributed to structural disorder and fluctuations in atomic positions from one crystallite to another.

$\text{Zn}_4\text{Si}_2\text{O}_7\text{Cl}_2$ Space group: $A 2 m m$ $a = 5.184172(12) \text{ \AA}$, $b = 17.7897(2) \text{ \AA}$, $c = 20.7771(3) \text{ \AA}$, $V = 1916.16(3) \text{ \AA}^3$, $Z = 8$					
atom	x	y	z	Occ.	$B_{\text{iso}} (\text{Å}^2)$
Zn1	0.804(7)	0.10882(18)	0.07742(16)	1	1.373(17)
Zn2	0.310(6)	0.16913(16)	0.14602(13)	1	1.373(17)
Zn3	0.293(7)	0.35377(19)	0.17182(15)	1	1.373(17)
Zn4	0.818(7)	0.40646(16)	0.08753(15)	1	1.373(17)
Cl1	0.709(7)	0	0.1347(6)	1	3.93(14)
Cl2	0.183(7)	0.3982(6)	0.2741(4)	1	3.93(14)
Cl3	0.780(7)	0.3271(5)	0	1	3.93(14)
Si1	0.282(8)	0.0778(5)	0	1	1.35(9)
Si2	0.294(7)	0.5	0.0742(5)	1	1.35(9)
Si3	0.794(7)	0.2566(4)	0.1806(3)	1	1.35(9)
O1	0.101(7)	0.2720(9)	0.1639(8)	1	0.49(11)
O2	0.695(7)	0.1201(11)	0	1	0.49(11)
O3	0.25*	0	0	1	0.49(11)
O4	0.181(7)	0.1101(9)	0.0514(7)	1	0.49(11)
O5	0.767(10)	0.25	0.25	1	0.49(11)
O6	0.203(7)	0.4155(8)	0.0982(8)	1	0.49(11)
O7	0.695(7)	0.1933(9)	0.1326(8)	1	0.49(11)
O8	0.626(8)	0.5	0.0828(12)	1	0.49(11)
O9	0.320(9)	0.5	0	1	0.49(11)
O10	0.764(7)	0.3111(8)	0.1481(6)	1	0.49(11)

SUPPORTING INFORMATION

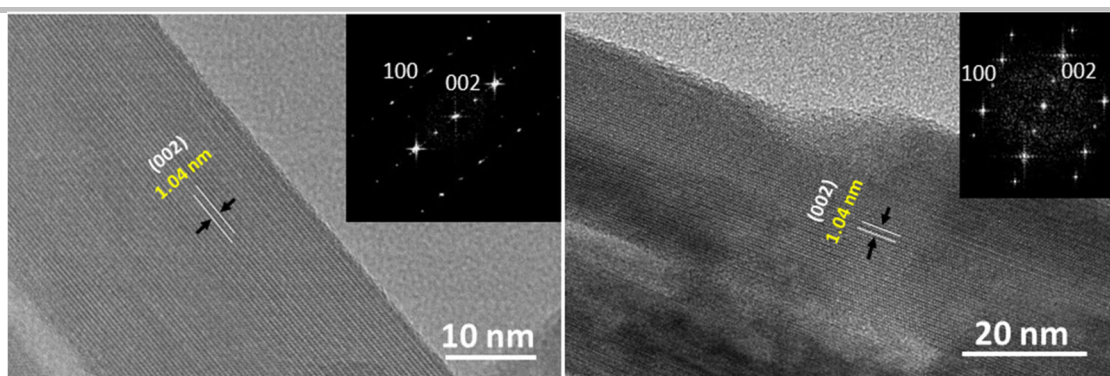


Figure S11. HRTEM images and corresponding FFT patterns of $\text{Zn}_4\text{Si}_2\text{O}_7\text{Cl}_2$ nanowires ([010] zone axis).

Table S6. Known compounds in the polar orthorhombic $A2mm$ space group

Sl. No.	Compound	Reference
1.	$\gamma\text{-Hg}_3\text{S}_2\text{Cl}_2$	<i>Acta Cryst.</i> 1968 , B24, 1661.
2.	$(\text{Na}(\text{H}_2\text{O})_2)_{0.25}(\text{MoO}_3)$	<i>Mater. Res. Bull.</i> 1986 , 21, 945.
3.	$\text{Tl}_5\text{Ba}_3\text{Sr}_5\text{Cu}_3\text{O}_{19}$	<i>J. Solid State Chem.</i> 1997 , 128, 150.
4.	$\text{Tl}_3\text{Sr}_8\text{Cu}_4(\text{CrO}_4)\text{O}_{15.9}$	<i>Eur. Phys. J. AP.</i> 1998 , 1, 285.
5.	$(\text{La}_{1.5}\text{Ca}_{0.5})(\text{CoO}_4)$	<i>J. Phys. Soc. Jpn.</i> 2008 , 77, 044601.

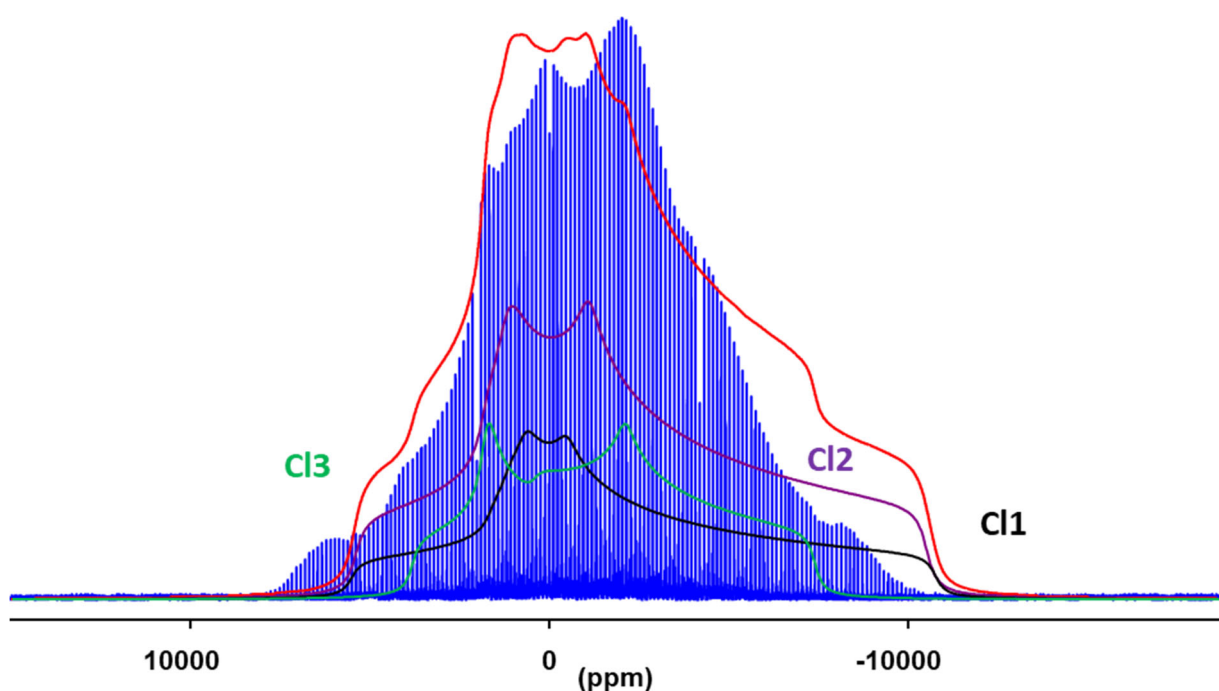


Figure S12. ^{35}Cl static experimental solid-state NMR spectrum of $\text{Zn}_4\text{Si}_2\text{O}_7\text{Cl}_2$ nanowires (blue) and calculated (red) signal from the 3 different Cl positions modeled by DFT according to the structure refined from PEDT. The variation range of the calculated lineshapes dominated by strong quadrupolar interactions (quadrupolar coupling constants ($17.4 \text{ MHz} < |^{\text{calc}}C_Q(^{35}\text{Cl})| < 18.2 \text{ MHz}$) is consistent with the experimental data.

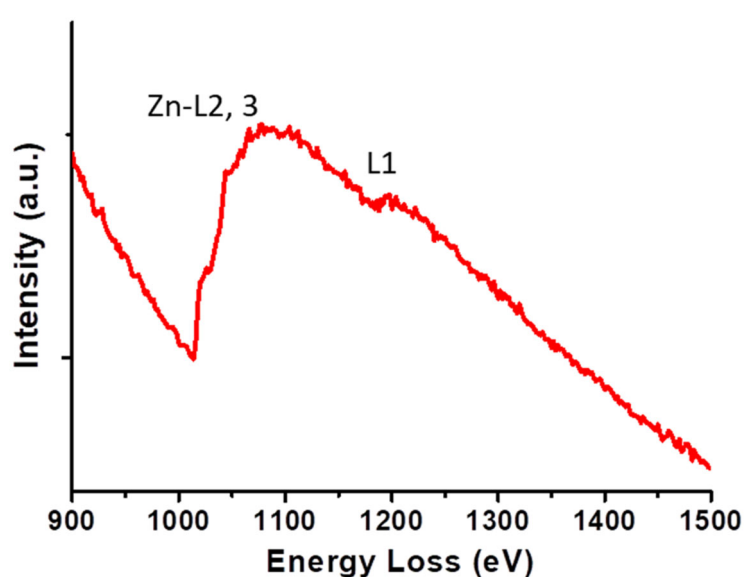


Figure S13. EELS spectrum of $\text{Zn}_4\text{Si}_2\text{O}_7\text{Cl}_2$ nanowires in the region of the Zn L_1 , L_2 and L_3 edges.

SUPPORTING INFORMATION

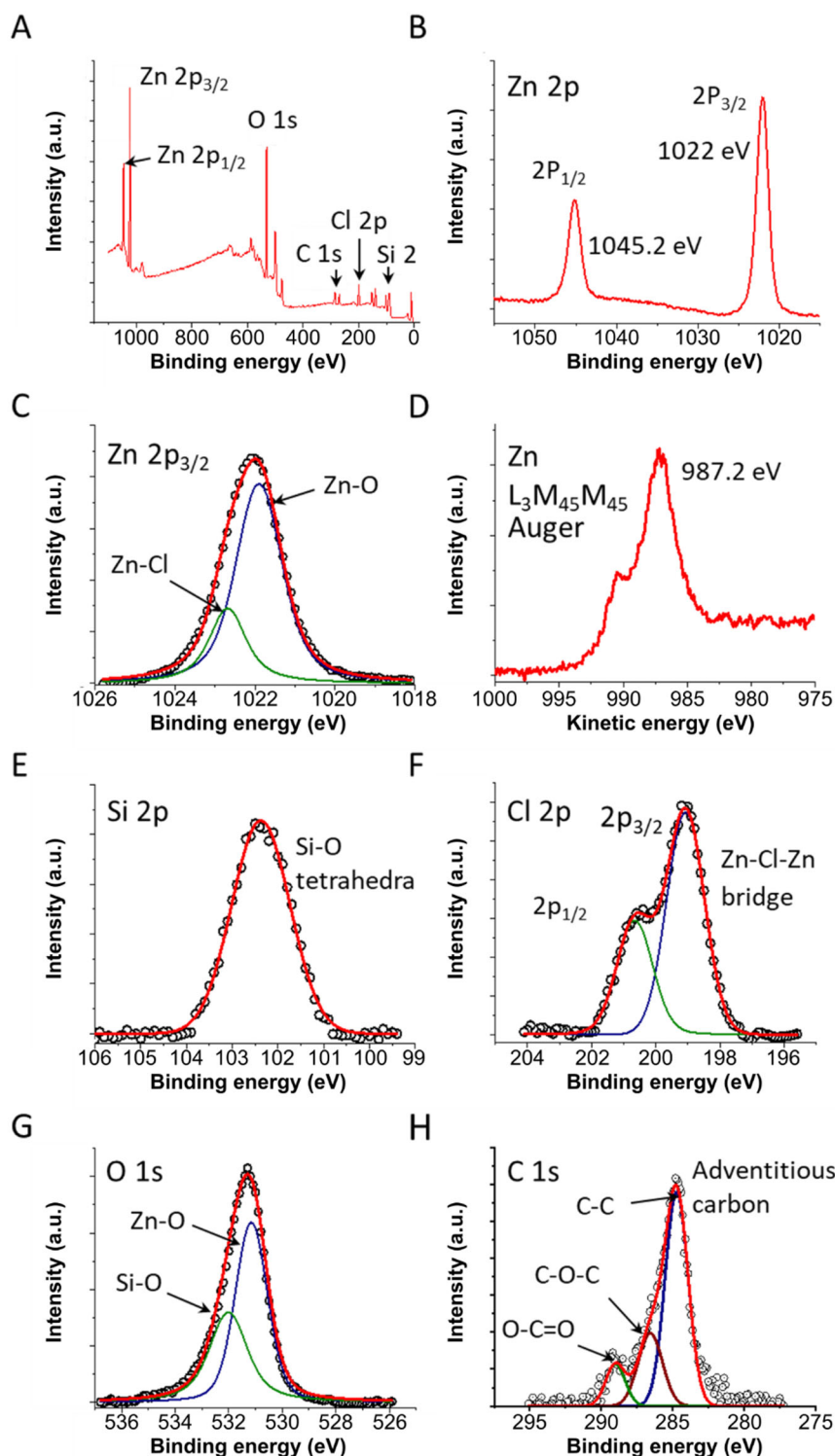


Figure S14. High resolution X-ray photoelectron spectra (XPS) of $\text{Zn}_4\text{Si}_2\text{O}_7\text{Cl}_2$ nanowires. (A) Survey spectrum. (B) Zn-2p core level with the characteristic 2p_{3/2} and 2p_{1/2} splitting. (C) Zn-2p_{3/2} in different chemical bonding (Zn-O and Zn-Cl) environments. (D) Characteristic Zn-L₃M_{4,5}M_{4,5} Auger spectrum. (E) Si-2p core level showing Si bonded to O. (F) Cl-2p core level with the characteristic splitting into 2p_{3/2} and 2p_{1/2}. (G) O-1s core level bonded to Zn and Si respectively. (H) C-1s core level showing adventitious

SUPPORTING INFORMATION

carbon. The spectra and valence band were corrected with respect to C-1s 284.8 eV. The parameters of the fit are summarized in **Table S7**. The Zn 2p_{3/2} and 2p_{1/2} peaks at ca. 1022 and 1045 eV with an expected 2:1 intensity ratio. The Zn 2p_{3/2} has two contributions at 1021.9 and 1022.7 eV corresponding to Zn-O and Zn-Cl respectively.^[24–26] The Zn L₃M_{4,5}M_{4,5} Auger peak was observed at a kinetic energy of 987.2 eV characteristic of the Zn²⁺ oxidation state.^[27,28] The Si 2p core level at 102.4 eV corresponds to Si⁴⁺O₄ tetrahedra.^[29–31] The deconvoluted Cl 2p_{3/2} and 2p_{1/2} peaks at 199.0 and 200.6 eV with an expected intensity ratio of 2:1 correspond to bridging Zn-Cl bonds. The O 1s core level shows two contributions at 531 and 532 eV corresponding to oxygen bonded to zinc and silicon respectively.^[32,33]

Table S7. XPS peak assignments fitted to Voigt function and corrected with respect to C-1s at 284.8 eV.

Core level	Binding energy (eV)	Assignments
Zn 2p _{3/2}	1022.0	-
Zn 2p _{1/2}	1045.2	-
Zn 2p _{3/2}	1021.9	Zn-O
Zn 2p _{3/2}	1022.7	Zn-Cl
Si 2p	102.4	Si-O (tetrahedra)
Cl 2p _{1/2}	199.0	Zn-Cl-Zn bridge
Cl 2p _{3/2}	200.6	Zn-Cl-Zn bridge
O 1s	531	O-Zn
O 1s	532	O- Si
C 1s	284.8	C-C
C 1s	286.4	C-O-C
C 1s	288.8	O-C=O

- Zn Auger Zn-L₃M_{4,5}M_{4,5} kinetic energy = 987.2 eV

SUPPORTING INFORMATION

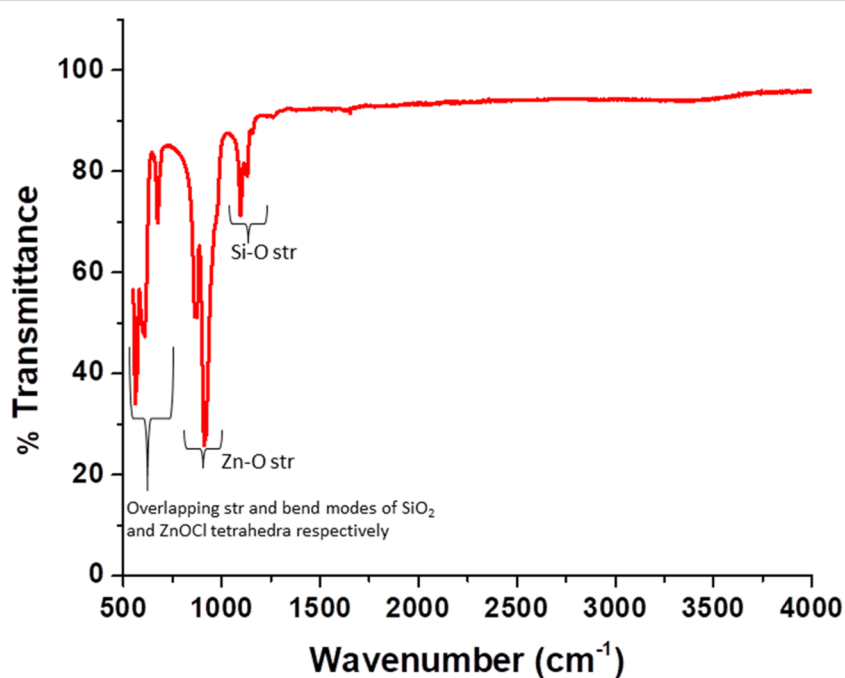


Figure S15. Infrared spectrum of $\text{Zn}_4\text{Si}_2\text{O}_7\text{Cl}_2$ nanowires showing the characteristic Si-O, Zn-O and bending modes of the SiO_2 and ZnO_3Cl tetrahedra respectively. Bands in the 1095-1160 cm^{-1} region are associated to the Si-O stretching modes.^[34] Doublet bands centered at 916 and 870 cm^{-1} are associated to the Zn-O stretching modes. The IR modes in 500-700 cm^{-1} are assigned to the overlapping stretching and bending modes of $(\text{SiO}_4)^{2-}$ and ZnO_3Cl tetrahedra, respectively.^[35,36]

SUPPORTING INFORMATION

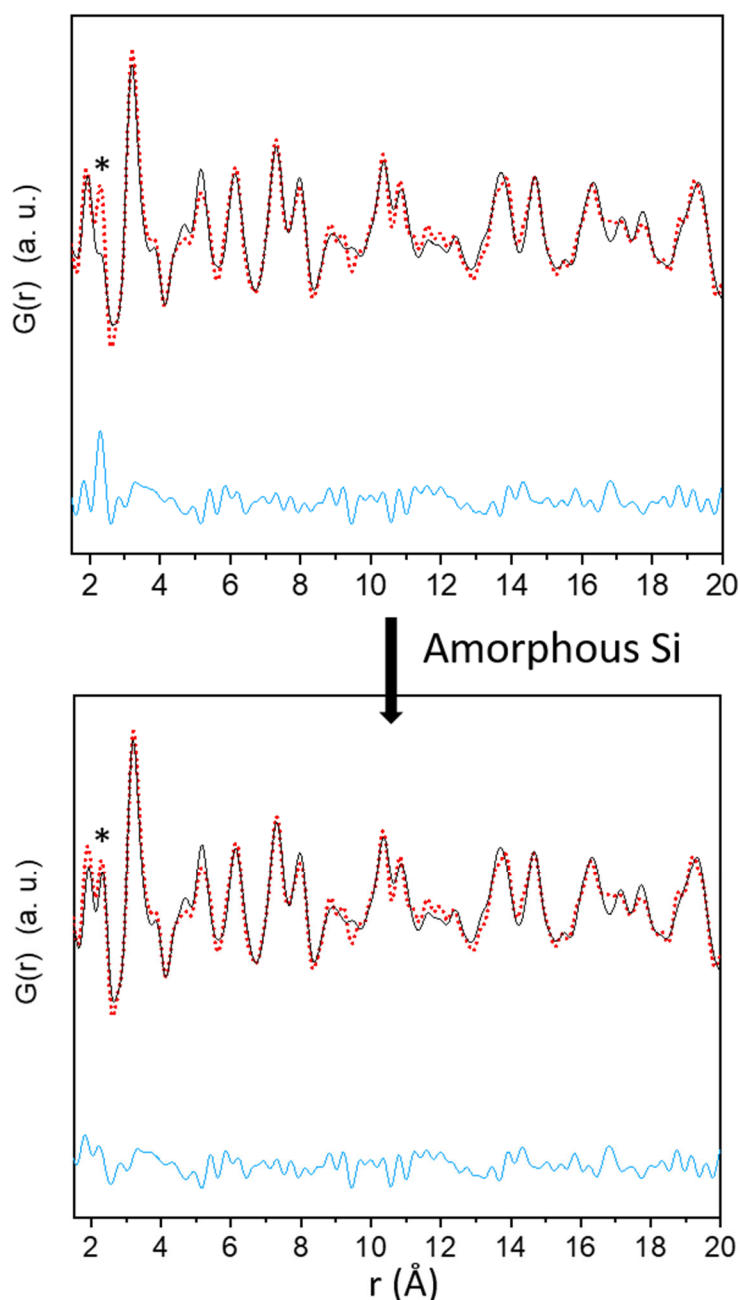


Figure S16. PDF analysis. Refinement from fixed PEDT atomic positions and cell parameters, with variable scale, isotropic thermal displacement and broadening factors lead to an acceptable fit ($R_w=28.1\%$) with pure $Zn_4Si_2O_7Cl_2$ (top), except for the peak at 2.30 \AA that can not be assigned to any distances in $Zn_4Si_2O_7Cl_2$. This impurity is amorphous since it has not been detected by XRD. Moreover, no additional correlation peak has been detected on the experimental PDF curve, confirming the very short order of this additional phase. Several phases ($NaCl$, $ZnCl_2$, Na_4Si_4 and Si) have been tested with an r_{cut} of 2.5 \AA to mimic the amorphous character. Among them, only $ZnCl_2$, Na_4Si_4 and Si present a calculated first correlation peak in the right distance range (2.19 , 2.37 , and 2.33 \AA , respectively). Amorphous silicon appears to be the closest one and thus the best option. Moreover, $ZnCl_2$ and Na_4Si_4 potentially remaining after the synthesis are highly soluble or should decompose during thorough

SUPPORTING INFORMATION

washing with water, so that amorphous Si is the only remaining possibility. Refinement including amorphous Si (scale factor of 0.2) lead to a better reliability factor ($R_w=23.8\%$), confirming the presence of this impurity.

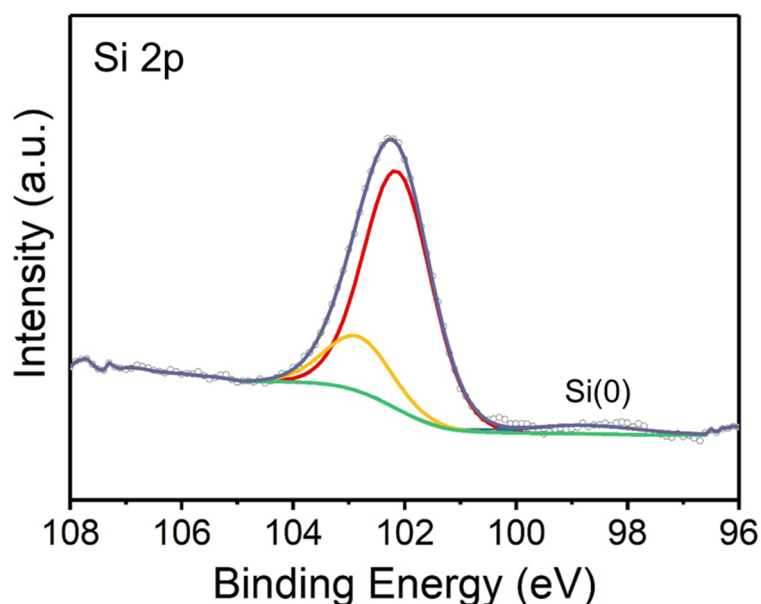


Figure S17. high- resolution Si-2p core level X-ray photoelectron spectrum showing the Si⁰ and Si⁴⁺ contributions fitted to retrieve a Si⁰/Si⁴⁺ value of 0.05.

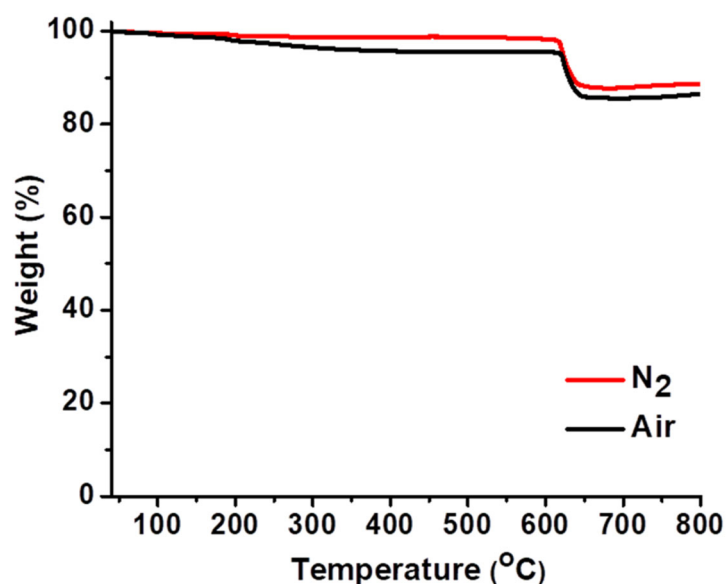


Figure S18. Thermogravimetric analysis of Zn₄Si₂O₇Cl₂ nanowires under (black) air and (red) nitrogen at a heating rate of 5 °C min⁻¹). The first weight loss of ~10 wt. % occurs at 600 °C in air or nitrogen. This is in good agreement with the decomposition into ZnO and silica from loss of chlorine, with an expected weight loss of ca. 11 wt. %.

SUPPORTING INFORMATION

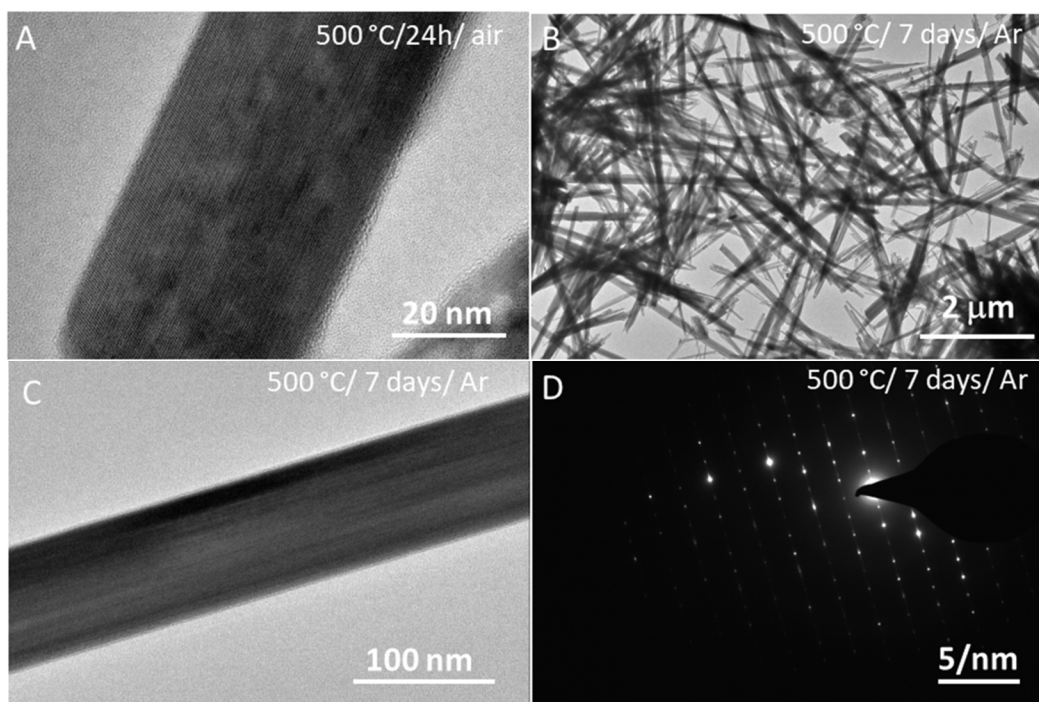


Figure S19. TEM images of $\text{Zn}_4\text{Si}_2\text{O}_7\text{Cl}_2$ nanowires exposed to different atmospheres: (A) annealed in air at 500 °C for 24 hours; (B, C) annealed for one week at 500 °C under argon. (D) shows the SAED pattern corresponding to the nanowire in (C).

SUPPORTING INFORMATION

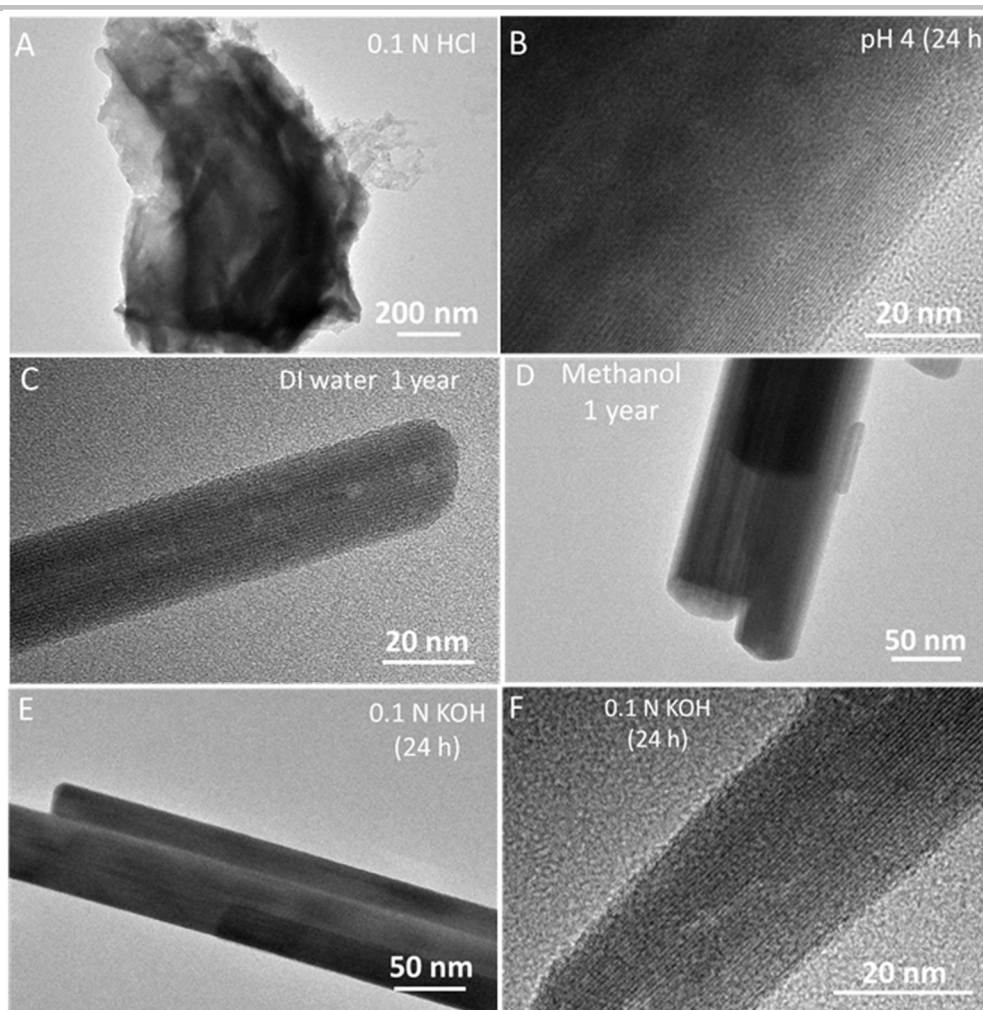


Figure S20. TEM images of $\text{Zn}_4\text{Si}_2\text{O}_7\text{Cl}_2$ nanowires exposed to different aqueous solutions: (A) 0.1 N HCl, (B) pH 4, (C) deionized water (DI) for 1 year, (D) methanol for 1 year, (E, F) 0.1 M KOH. The nanowires show no degradation for one year in water or methanol and high stability in alkaline conditions (0.1 N KOH). The compound decomposes in more acidic medium at e.g. 0.1 M HCl, which is assigned to amorphization, probably into silica or a zinc silicate.

SUPPORTING INFORMATION

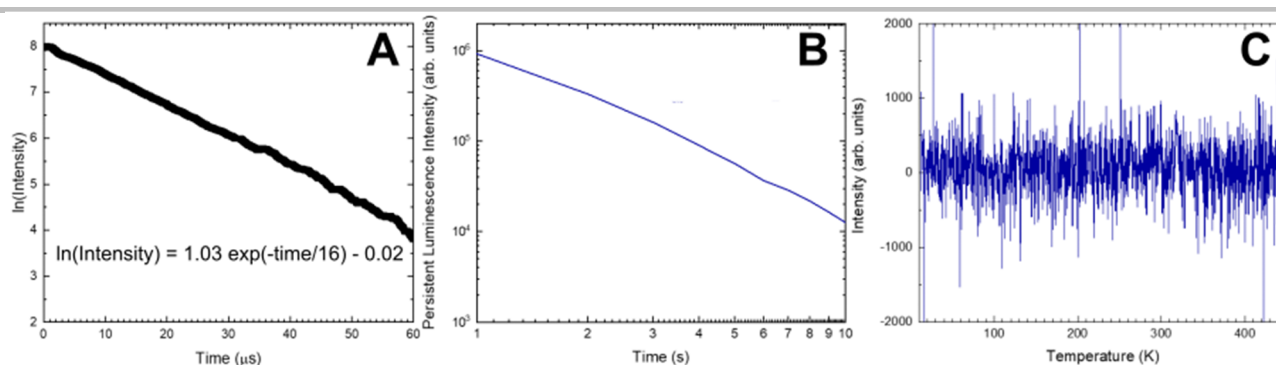


Figure S21. (A) Luminescence decay of the 2.8 eV emission at room temperature, with excitation at 230 nm. Exponential fitting yields a long lifetime of 16 μ s. (B) Emission at 13 K after excitation at 254 nm for 1 min, showing long duration afterglow. (C) Thermoluminescence after excitation at 254 nm for 10 min at 13 K, showing no glow peak. These three features indicate the presence of shallow defects.

Table S8. Atomic positions of $\text{Zn}_4\text{Si}_2\text{O}_7\text{Cl}_2$ structure after full geometry optimization leading to the unit cell parameters: $a=5.2648 \text{ \AA}$ $b=18.0190 \text{ \AA}$ $c=20.9947 \text{ \AA}$ in space group $A2mm$.

Atom	x	y	z
Zn1	0.8109	0.1087	0.0804
Zn2	0.3098	0.1729	0.1425
Zn3	0.3091	0.3572	0.1736
Zn4	0.8157	0.4057	0.0893
Cl1	0.7189	0	0.1338
Cl2	0.2176	0.4040	0.2719
Cl3	0.7607	0.3340	0
Si1	0.3073	0.0893	0
Si2	0.3075	0.5	0.0762
Si3	0.8048	0.2600	0.1743
O1	0.1106	0.2641	0.1597
O2	0.6130	0.1072	0
O3	0.2455	0	0
O4	0.1746	0.1248	0.0644
O5	0.7396	0.25	0.25
O6	0.1773	0.4254	0.1073
O7	0.6769	0.1901	0.1351
O8	0.6170	0.5	0.0880
O9	0.2358	0.5	0
O10	0.6685	0.3388	0.1538

SUPPORTING INFORMATION

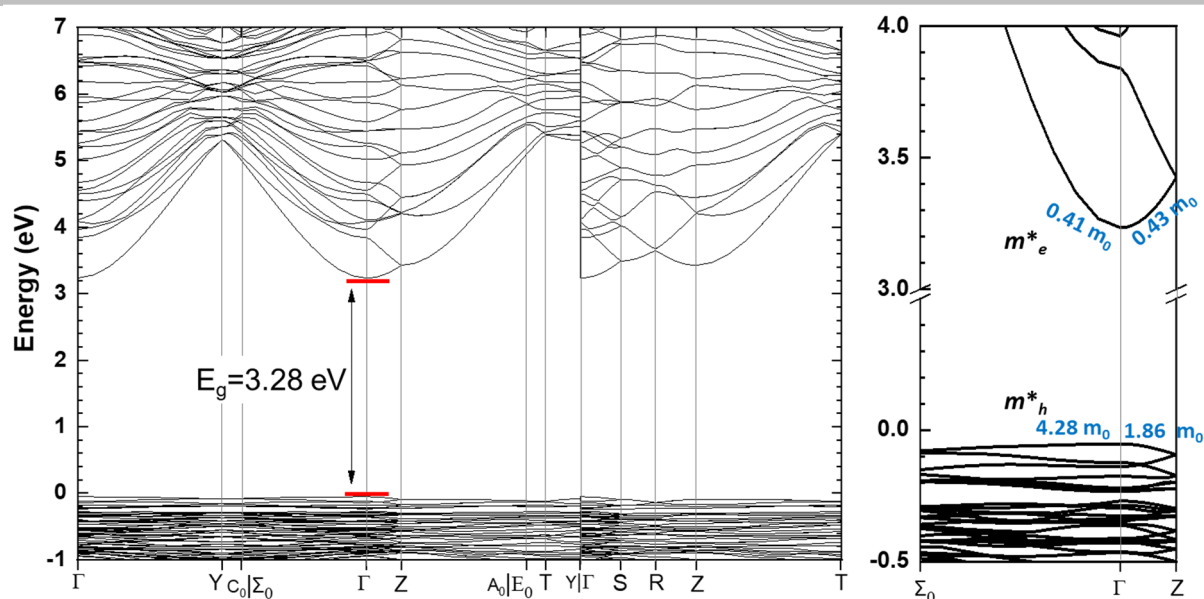


Figure S22. Band structure of $\text{Zn}_4\text{Si}_2\text{O}_7\text{Cl}_2$ with the valence band maximum (VBM) and conduction band minimum (CBM) highlighted. Both the CBM and the VBM are located at k point Γ thus indicating a direct ($\Gamma \rightarrow \Gamma$) band gap of 3.28 eV. The zoom in around Γ on the right is also displayed Figure 3C and shows the effective masses of electrons (m_e^*) and holes (m_h^*) calculated along different directions.

Table S9. Effective masses of electrons (m_e^*) and holes (m_h^*) for $\text{Zn}_4\text{Si}_2\text{O}_7\text{Cl}_2$ along different directions in the reciprocal space according to the PBE functional (in units of electron mass at rest, m_0). The effective masses have been calculated^[37] using the following equation near the CBM and VBM :

$$\left(\frac{1}{m^*}\right)_{ij} = \frac{1}{\hbar^2} \frac{\partial^2 E_n(k)}{\partial k_i \partial k_j}$$

where $E_n(k)$ corresponds to the n -th electronic band in k -space.

The band structure shows very different dispersion of the bands at CBM and at VBM suggesting quite different mobility of electrons and holes. Since the VBM and CBM are located at Γ , we investigated the directions $\Gamma \rightarrow Z$, $\Gamma \rightarrow \Sigma_0$ and $\Gamma \rightarrow S$ very near the Γ point. Prior to the effective masses extraction, the self-consistent electronic calculation was followed by a non-self-consistent calculation along the high symmetry lines with a fine spacing of 0.02 \AA^{-1} of k points in reciprocal space. The more dispersive CBM bands lead to low electron effective mass with $m_e^* < 0.5 m_0$ (m_0 stands for the electron mass at rest) for all directions (see **Table S9** below). On another hand, the flatter VBM bands lead to larger m_h^* with anisotropic values, the lowest mass being $1.86 m_0$ and the largest one $4.23 m_0$.

	$m_h^* (m_0)$	$m_e^* (m_0)$
$\Gamma \rightarrow Z$	1.865	0.429
$\Gamma \rightarrow \Sigma_0$	4.279	0.415
$\Gamma \rightarrow S$	2.168	0.429

SUPPORTING INFORMATION

In a recent high-throughput theoretical study including binary and ternary oxides, very low electron effective mass m_e^* have been obtained for cations between group 12 and group 15 in rows 4 and 5 which include $(n-1)d^{10}ns^0np^0$ cations such as Zn^{2+} as found in our compound.^[38] In particular, it was shown that the lowest effective masses are correlated with a strong s orbital character of the CBM with efficient hybridization with oxygen. These features are observed in our case (see PDOS in **Figure S19** below with Zn 4s and O3 (2p) states) although the mixed anion environment of Zn with the contribution of chlorine should be also considered.

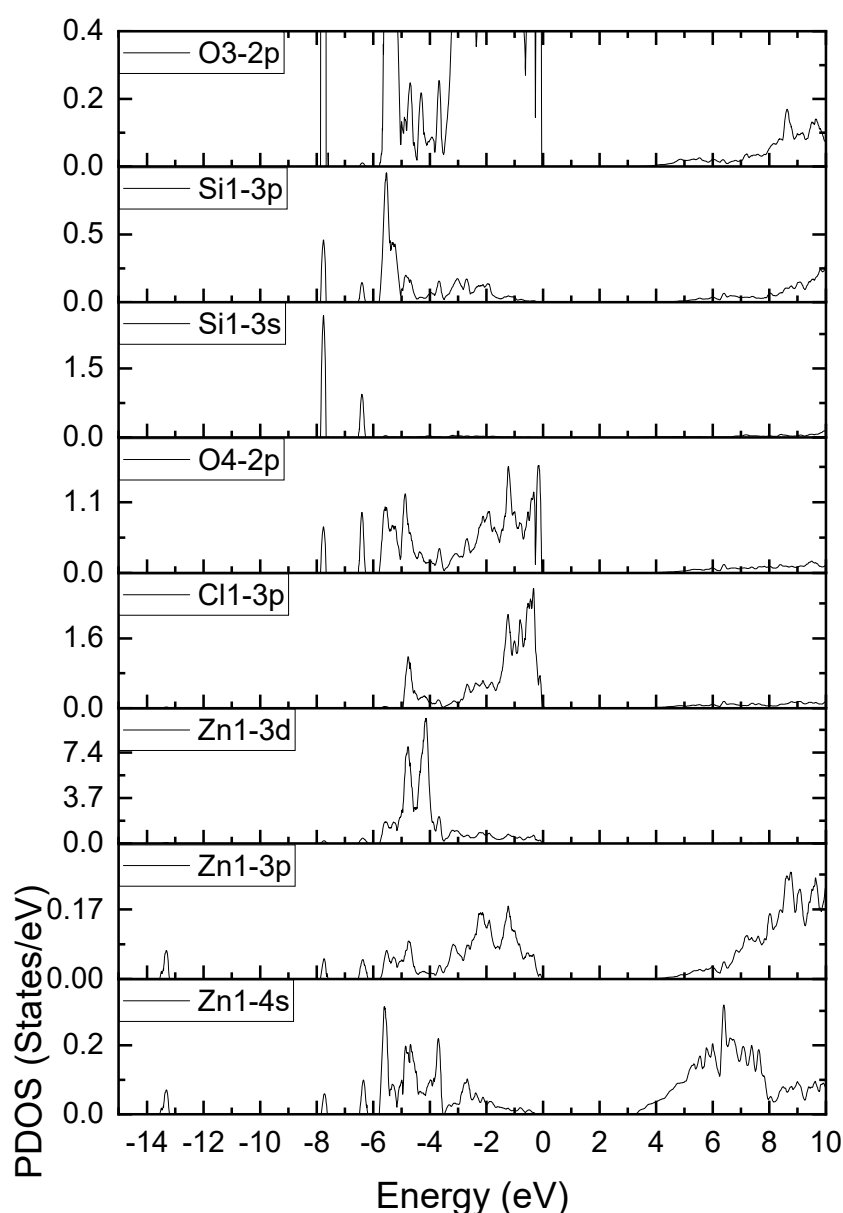


Figure S23. Projected Density of States (PDOS) for $Zn_4Si_2O_7Cl_2$. PDOS is shown for a representative portion of the structure including Zn(1) connected to Cl(1) and O(3). Si(1) is shown with O(4), the later connects exclusively Si atoms). The Fermi level is set to 0 eV.

SUPPORTING INFORMATION

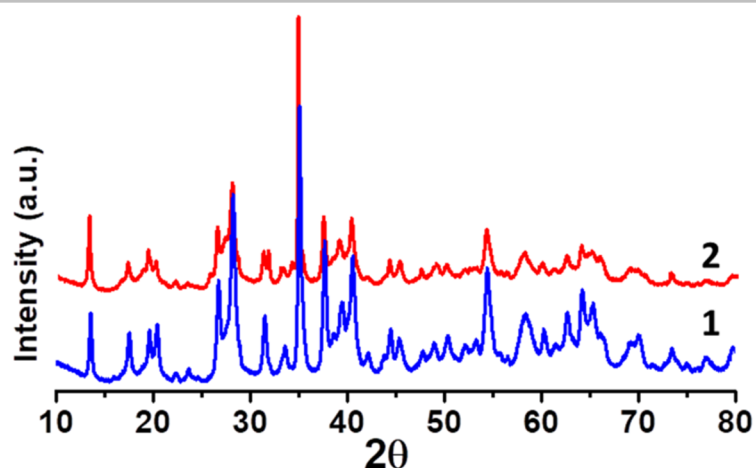


Figure S24. Powder XRD patterns of (1) p-type $\text{Zn}_4\text{Si}_2\text{O}_7\text{Cl}_2$ synthesized in glass and (2) n-type $\text{Zn}_4\text{Si}_2\text{O}_7\text{Cl}_2$ synthesized in a glassy carbon crucible.

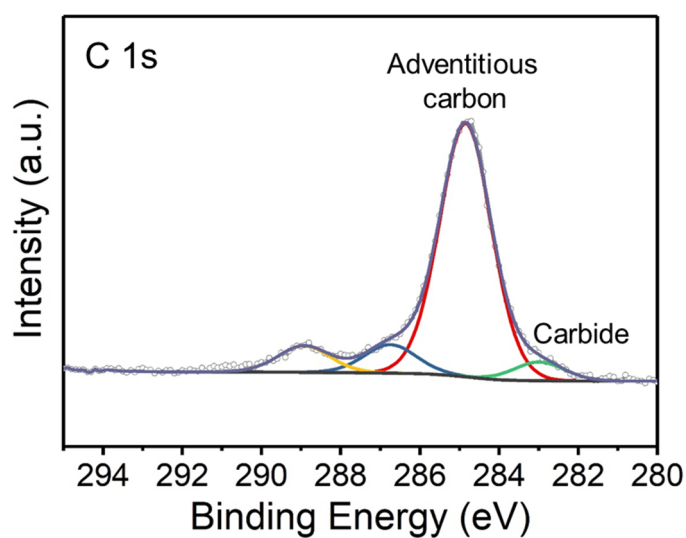


Figure S25. Fitted high-resolution C 1s core level X-ray photoelectron spectra of carbon-doped $\text{Zn}_4\text{Si}_2\text{O}_7\text{Cl}_2$. The component at ca. 282.8 eV is characteristic of carbide species. The intensities were normalized using Scofield factors. The atomic ratio of carbide-related C versus Zn is evaluated at ca. 0.1.

SUPPORTING INFORMATION

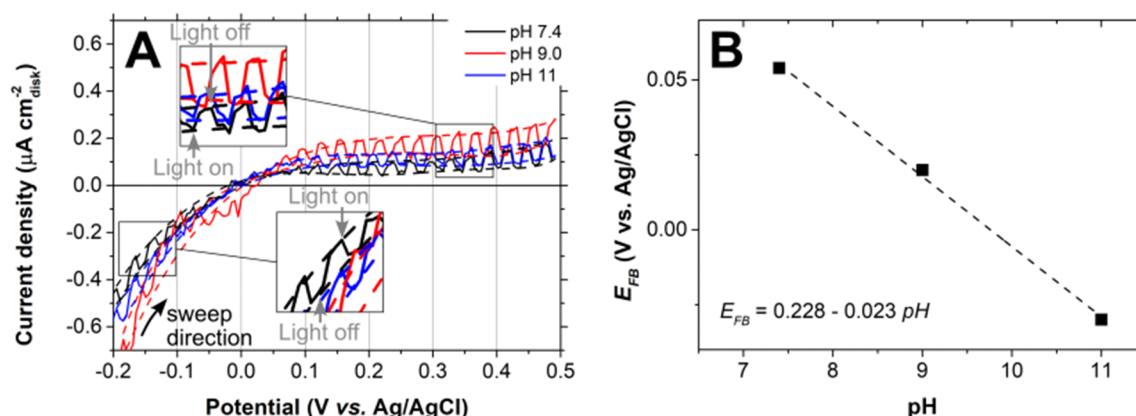


Figure S26. (A) Linear sweep voltammetry under chopped light (280 W Xe arc lamp, no energy filter, chop frequency $1/60 \text{ s}^{-1}$) at different pH values and 0.5 mV s^{-1} scan rate. Dashed lines indicate branches under illumination (high absolute currents) and under dark (low absolute currents). (B) Flat band potential evaluated at the crossover of the LSV branches in (A) under illumination and dark conditions.

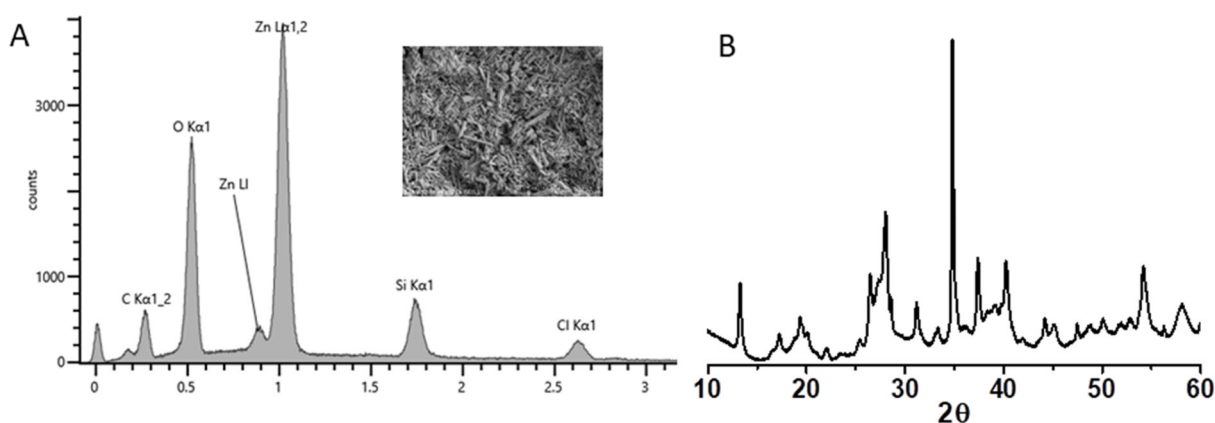


Figure S27. (A) EDS and (B) XRD pattern of electrode after the photoelectrochemical measurements (3 h of chronopotentiometry under chopped 280W Xe light at -0.05 V/RHE in a $0.1 \text{ M Na}_2\text{SO}_4$ electrolyte). The electrode was rinsed by dipping in water several times and dried at $60 \text{ }^\circ\text{C}$ to wash the electrolyte residues.

SUPPORTING INFORMATION

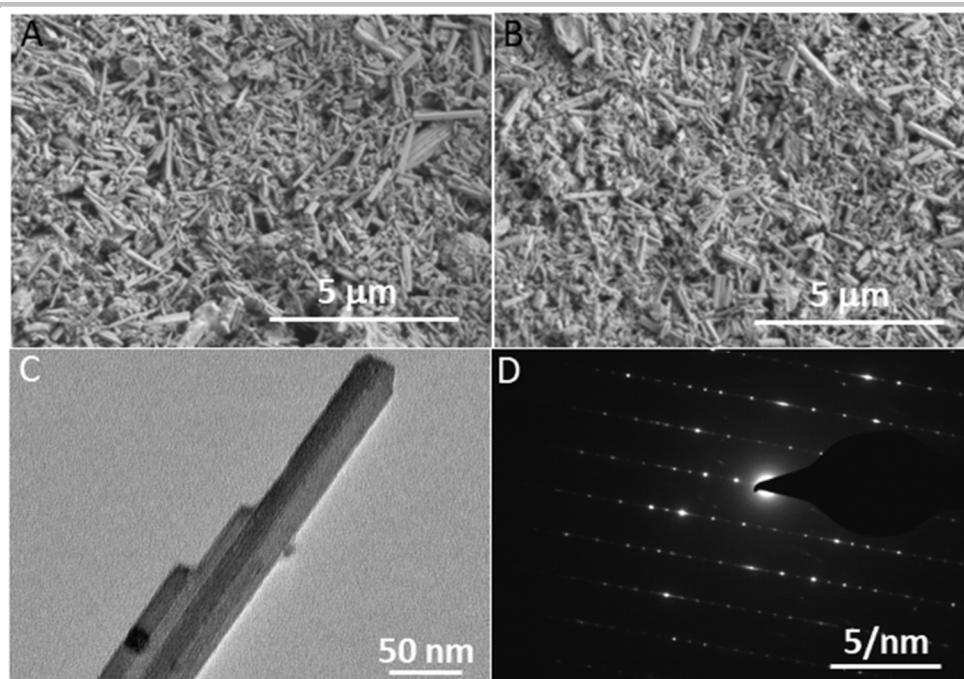


Figure S28. SEM, TEM and electron diffraction characterization of $\text{Zn}_4\text{Si}_2\text{O}_7\text{Cl}_2$ nanowires after 3 h of chronopotentiometry under chopped 280W Xe light at -0.05 V/RHE in a 0.1 M Na_2SO_4 electrolyte.

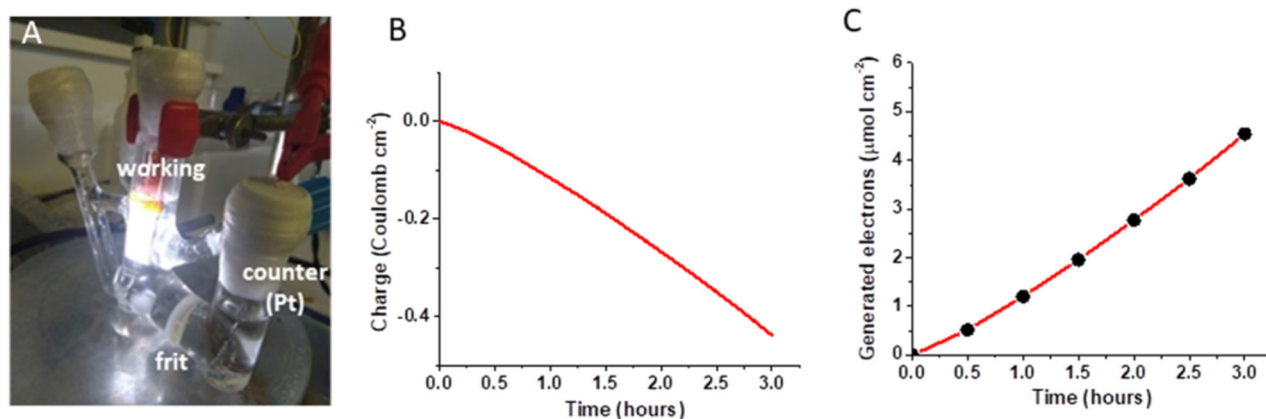


Figure S29. (A) Photoelectrochemical cell setup used in the experiments. (B) Charge versus time plot of $\text{Zn}_4\text{Si}_2\text{O}_7\text{Cl}_2$ photocathode at -0.2V vs RHE. (C) Generated electrons at different time intervals derived from the charge-time plot at -0.2V vs RHE. Electrolyte = 0.1 M Na_2SO_4 , light source = 280 W Xenon arc lamp.

SUPPORTING INFORMATION

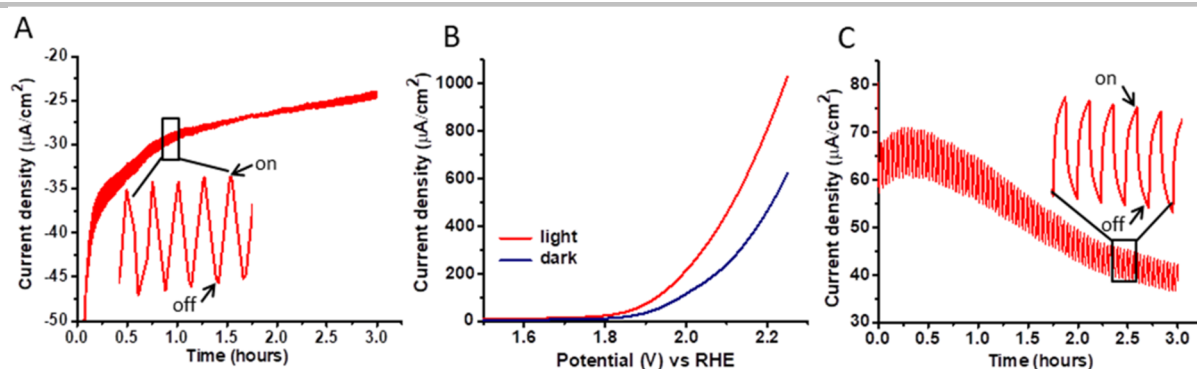


Figure S30. Photoelectrochemical properties of C-doped Zn₄Si₂O₇Cl₂ nanowires. (A) Chopped-light chronoamperometric measurement at a bias of -0.05 V/RHE (shutter time = 0.5 min) showing quenched cathodic current under illumination. (B) Linear sweep voltammetry of Zn₄Si₂O₇Cl₂ nanowire photoelectrode at a scan rate of 20 mV s⁻¹. (C) Chopped-light chronoamperometric measurement at a bias of 1.95 V/RHE (shutter time = 1 min). Electrolyte = 0.1 M Na₂SO₄, light source = 280 W Xe arc lamp.

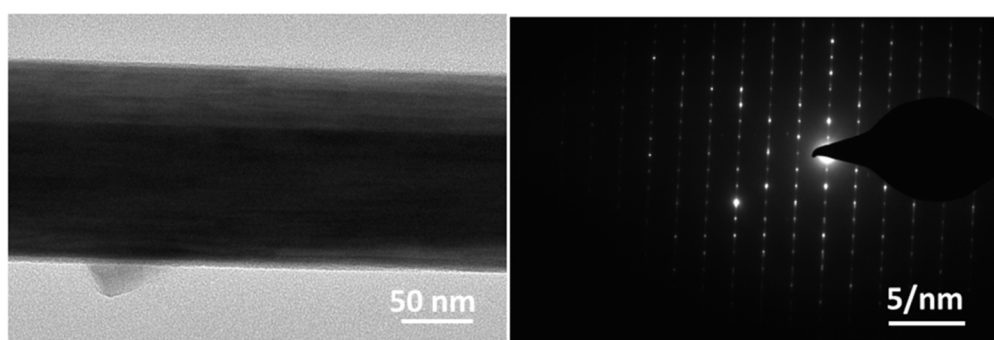


Figure S31. TEM image and corresponding selected area electron diffraction (SAED) pattern of the Zn₄Si₂O₇Cl₂ nanowires synthesized in a glassy carbon crucible and after 3 hours of oxygen evolution reaction at 1.95 V/RHE (shutter time = 1 min) in 0.1 M Na₂SO₄, showing the stability of the material in oxidation conditions.

References

- [1] X. Ma, F. Xu, T. M. Atkins, A. M. Goforth, D. Neiner, A. Navrotsky, S. M. Kauzlarich, *Dalt. Trans.* **2009**, 10250.
- [2] A. Courac, Y. Le Godec, C. Renero-Lecuna, H. Moutaabbid, R. Kumar, C. Coelho-Diogo, C. Gervais, D. Portehault, *Inorg. Chem.* **2019**, *58*, 10822.
- [3] R. Carvajal, "No Title," can be found under <https://www.ill.eu/sites/fullprof/>, n.d.
- [4] P. Juhás, T. Davis, C. L. Farrow, S. J. L. Billinge, *J. Appl. Crystallogr.* **2013**, *46*, 560.
- [5] C. L. Farrow, P. Juhas, J. W. Liu, D. Bryndin, E. S. Boin, J. Bloch, T. Proffen, S. J. L. Billinge, *J. Phys. Condens. Matter* **2007**, *19*, DOI 10.1088/0953-8984/19/33/335219.
- [6] L. Palatinus, P. Brázda, M. Jelínek, J. Hrdá, G. Steciuk, M. Klementová, *Acta Crystallogr. Sect. B* **2019**, *75*, 512.
- [7] V. Petříček, M. Dušek, L. Palatinus, *Zeitschrift für Krist. - Cryst. Mater.* **2014**, *229*, 345.
- [8] L. Palatinus, G. Chapuis, *J. Appl. Crystallogr.* **2007**, *40*, 786.
- [9] L. Palatinus, C. A. Corrêa, G. Steciuk, D. Jacob, P. Roussel, P. Boullay, M. Klementová, M. Gemmi, J. Kopeček, M. C. Domeneghetti, F. Cámara, V. Petříček, *Acta Crystallogr. Sect. B Struct. Sci. Cryst. Eng. Mater.* **2015**, *71*, 740.
- [10] M. Watanabe, E. Okunishi, K. Ishizuka, *Microsc. Anal.* **2009**, *23*, 5.
- [11] R. Siegel, T. T. Nakashima, R. E. Wasylshen, *Concepts Magn. Reson. Part A* **2005**, *26A*, 47.
- [12] D. Massiot, F. Fayon, M. Capron, I. King, S. Le Calvé, B. Alonso, J.-O. Durand, B. Bujoli, Z. Gan, G. Hoatson, *Magn. Reson. Chem.* **2002**, *40*, 70.
- [13] N. Hirayama, H. Nakata, H. Wakayama, S. Nishioka, T. Kanazawa, R. Kamata, Y. Ebato, K. Kato, H. Kumagai, A. Yamakata, K. Oka, K. Maeda, *J. Am. Chem. Soc.* **2019**, *141*, 17158.
- [14] S. Nishioka, T. Kanazawa, K. Shibata, Y. Tsujimoto, H.-C. zur Loye, K. Maeda, *Dalt. Trans.* **2019**, *48*, 15778.
- [15] G. Kresse, D. Joubert, *Phys. Rev. B* **1999**, *59*, 1758.
- [16] P. E. Blöchl, *Phys. Rev. B* **1994**, *50*, 17953.
- [17] G. Kresse, J. Furthmüller, **2012**.
- [18] J. P. Perdew, K. Burke, M. Ernzerhof, *Phys. Rev. Lett.* **1996**, *77*, 3865.
- [19] Y. Hu, Y. Pan, Z. Wang, T. Lin, Y. Gao, B. Luo, H. Hu, F. Fan, G. Liu, L. Wang, *Nat. Commun.* **2020**, *11*, 1.
- [20] C. Pickard, F. Mauri, *Phys. Rev. B* **2001**, *63*, 245101.
- [21] C. Bonhomme, C. Gervais, F. Babonneau, C. Coelho, F. Pourpoint, T. Azaïs, S. E. Ashbrook, J. M. Griffin, J. R. Yates, F. Mauri, C. J. Pickard, *Chem. Rev.* **2012**, *112*, 5733.
- [22] P. Giannozzi, S. Baroni, N. Bonini, M. Calandra, R. Car, C. Cavazzoni, D. Ceresoli, G. L. Chiarotti, M. Cococcioni, I. Dabo, A. Dal Corso, S. de Gironcoli, S. Fabris, G. Fratesi, R. Gebauer, U. Gerstmann, C. Gougoussis, A. Kokalj, M. Lazzeri, L. Martin-Samos, N. Marzari, F. Mauri, R. Mazzarello, S. Paolini, A. Pasquarello, L. Paulatto, C. Sbraccia, S. Scandolo, G. Sclauzero, A. P. Seitsonen, A. Smogunov, P. Umari, R. M. Wentzcovitch, *J. Phys. Condens. Matter* **2009**, *21*, 395502.
- [23] L. Palatinus, A. Van Der Lee, *J. Appl. Crystallogr.* **2008**, *41*, 975.
- [24] J. C. Klein, D. M. Hercules, *J. Catal.* **1983**, *82*, 424.
- [25] R. D. Seals, R. Alexander, L. T. Taylor, J. G. Dillard, *Inorg. Chem.* **1973**, *12*, 2485.
- [26] E. M. Olegario, C. M. O. Pelicano, L. A. Dahonog, H. Nakajima, *Mater. Res. Express* **2018**, *6*, 15005.
- [27] G. Schön, *J. Electron Spectros. Relat. Phenomena* **1973**, *2*, 75.
- [28] L. S. Dake, D. R. Baer, J. M. Zachara, *Surf. Interface Anal.* **1989**, *14*, 71.
- [29] R. van Weeren, E. A. Leone, S. Curran, L. C. Klein, S. C. Danforth, *J. Am. Ceram. Soc.* **1994**, *77*, 2699.
- [30] W. A. M. Aarnink, A. Weishaupt, A. van Silfhout, *Appl. Surf. Sci.* **1990**, *45*, 37.
- [31] Z. M. Wang, Q. Fang, J. Y. Zhang, J. X. Wu, Y. Di, W. Chen, M. L. Chen, I. W. Boyd, *Thin Solid Films* **2004**, *453–454*, 167.
- [32] D. W. Langer, C. J. Vesely, *Phys. Rev. B* **1970**, *2*, 4885.
- [33] D. Sprenger, H. Bach, W. Meisel, P. Gütllich, *J. Non. Cryst. Solids* **1990**, *126*, 111.
- [34] E. R. Lippincott, A. V Valkenburg, C. E. Weir, E. N. Bunting, *J. Res. Natl. Bur. Stand. (U. S.)* **1958**, *61*, 61.
- [35] G. Heiland, H. Lüth, *Solid State Commun.* **1967**, *5*, 199.
- [36] F. Boccuzzi, C. Morterra, R. Scala, A. Zecchina, *J. Chem. Soc. Faraday Trans. 2 Mol. Chem. Phys.* **1981**, *77*, 2059.
- [37] V. Wang, N. Xu, J. C. Liu, G. Tang, W.-T. Geng, "VASPKIT: A User-friendly Interface Facilitating High-

SUPPORTING INFORMATION

throughput Computing and Analysis Using VASP Code,” **2019**.

[38] G. Hautier, A. Miglio, D. Waroquiers, G. Rignanese, X. Gonze, *Chem. Mater.* **2014**, 26, 5447.

[39] Y. Matsumoto, *J. Solid State Chem.* **1996**, 126, 227.